Reversible One-way Lipid Transfer at ER–Autophagosome Membrane Contact Sites via Bridge-like Lipid Transfer Protein Atg2

Li Hao[1], Tomoki Midorikawa[1], Yuta Ogasawara[4], Yutaro Hama[4], Huichao Lang[1], Nobuo N. Noda[4], Kuninori Suzuki[1,2,3,*]

[1]Department of Integrated Biosciences, Graduate School of Frontier Sciences, The University of Tokyo, Kashiwa, Japan

[2]Collaborative Research Institute for Innovative Microbiology, The University of Tokyo, Tokyo, Japan

[3]Life Science Data Research Center, The University of Tokyo, Kashiwa, Japan

[4]Institute for Genetic Medicine, Hokkaido University, Sapporo, Japan.

*Corresponding author: Kuninori Suzuki, kuninori@k.u-tokyo.ac.jp

Keywords: Atg2, autophagosome formation, bridge-like lipid transport, *in vivo* observation, lipid dynamics, membrane contact sites

Abbreviations

ARS, autophagy-related structure; Cryo-EM, cryo-electron microscope; DOPE, 1,2-dioleoyl-sn-glycero-3-phosphoethanolamine; ER, endoplasmic reticulum; ERES, ER exit site; FRAP, fluorescence recovery after photobleaching; GFP, green fluorescent protein; IM, isolation membrane; LTP, lipid transfer protein; mApe1, mature Ape1; MCS, membrane contact site; MD, molecular dynamics; MEF, mouse embryonic fibroblasts; mNG, monomeric NeonGreen; ORP, oxysterol-binding protein-related protein; OSBP, oxysterol-binding protein; OSW-1, orsaponin; PAS, pre-autophagosomal structure/phagophore assembly site; PM, plasma membrane; POPC, 1-palmitoyl-2-oleoyl-glycero-3-phosphocholine; prApe1, precursor Ape1; R18, octadecyl rhodamine B; RBG, repeating β-groove; WT, wild-type

Abstract

Bridge-like lipid transfer proteins (LTPs) contain a repeating β-groove domain and long hydrophobic grooves that act as bridges at membrane contact sites (MCSs) to efficiently transfer lipids. Atg2 is one such bridge-like LTP essential for autophagosome formation, during which a newly synthesized isolation membrane (IM) emerges and expands through lipid supply. However, studies on Atg2-mediated lipid transfer are limited to *in vitro* studies due to the lack of a suitable probe for monitoring phospholipid dynamics *in vivo*. Here, we characterized the lipophilic dye octadecyl rhodamine B (R18), which reached the endoplasmic reticulum (ER) through the actions of flippases and oxysterol-binding protein-related proteins. Using R18, we demonstrated phospholipid transfer from the ER to the IM during autophagy *in vivo*. Upon autophagy termination, we observed reversible phospholipid flow from the IM to the ER in response to environmental changes. Our findings highlight the critical role of bridge-like LTPs in MCS-mediated phospholipid homeostasis.

Introduction

Phospholipids are key constituents of various organelle membranes in eukaryotic cells. They are regulated asymmetrically and heterogeneously to form permeability barriers that separate organelles from their surroundings, creating distinct compartments. This organization facilitates the segregation and regulation of numerous reactions within cells. Cells maintain lipid homeostasis in organelle membranes by actively translocating and transferring lipids, ensuring optimal membrane function.

Membranes exchange phospholipids with each other via vesicular and nonvesicular pathways. In vesicular trafficking, vesicles transport lipids through secretory and endocytic pathways[1]. However, this process has several limitations. First, the quantity and rate at which vesicles deliver lipids are insufficient for organelle biogenesis[2]. Second, lipid transfer occurs in organelles that do not receive vesicles[3]. Therefore, it is plausible that pathways involved in the transport of phospholipids via mechanisms other than vesicular transport are crucial for maintaining cellular functions[4]. Nonvesicular trafficking primarily relies on lipid transfer proteins (LTPs) at membrane contact sites (MCSs), where the two organelles physically interact. Lipid transfer at these sites typically affects the functions of either organelle alone or both organelles[5-7]. The most well-characterized LTPs have a box-like structure with a hydrophobic core, allowing them to hold one or a few lipids[7]. These proteins transport lipids by first docking onto the donor membrane, extracting specific lipids. They diffuse through the cytoplasm before inserting the lipids into the acceptor membrane[7]. Recent studies have identified a new class of bridge-like LTPs characterized by repeating β-groove (RBG) domains and extended hydrophobic grooves[8, 9]. These large structures allow LTPs to bridge MCSs and facilitate efficient lipid transfer[4]. Five RBG proteins—Vps13, Atg2, BLTP1 (Tweek/Csf1/KIAA1109), BLTP2 (Hob/Fmp27/KIAA0100), and BLTP3 (SHIP164)[9-12]—have been identified in eukaryotes.

Among the bridge-like LTPs, Atg2 plays a critical role in macroautophagy (herein referred to as autophagy)[13-15]. Autophagy is a universally conserved intracellular degradation pathway that plays an essential role in cell homeostasis and stress responses[16]. It relies on the reorganization of lipid membranes to form an isolation membrane (IM) between the endoplasmic reticulum (ER) and vacuole, which contains engulfed cytoplasmic components. The IM then closes to become an autophagosome, enclosing damaged organelles or protein aggregates for degradation in vacuoles or lysosomes[17-19]. Atg2 forms a complex with Atg18 and the scramblase Atg9 at the edge of the expanding IM during autophagosome formation[20-23]. Additionally, a hydrophobic cavity in the N-terminal region of Atg2 directly tethers Atg2 to the ER, particularly the ER exit site (ERES), which is considered a key hub for autophagosome biogenesis[24, 25]. Previous *in vitro* studies on the crystal structure of yeast Atg2 suggest that it directly participates in phospholipid transfer at the ER–IM MCS[26]. However, the organelles responsible for the lipid supply for IM expansion are unknown [26-30].

Considerable progress has recently been made in our understanding of nonvesicular

lipid transport. However, a significant gap persists in our understanding of direct lipid transfer in living cells. Most evidence supporting the Atg2-mediated lipid transfer model is largely based on *in vitro* studies[14, 15, 26, 31, 32]. The lack of tools for determining lipid transfer in living cells also raises concerns about the validity of conclusions drawn from such studies.

In this study, we identified the lipophilic dye octadecyl rhodamine B (R18), which undergoes nonvesicular transport from the plasma membrane (PM) through the ER to autophagy-related structures (ARSs), including IMs, autophagosomes, and autophagic bodies. Using R18, we investigated lipid transfer from the ER to the IM during autophagosome formation. Our time-lapse imaging analysis also revealed rapid lipid supply accompanied by IM expansion. Our study demonstrated lipid transfer from the ER to the IM and strongly suggested that the ER is the primary source of lipids for IM expansion. Furthermore, we developed a repletion assay using a nutrient-rich medium to terminate autophagy under confocal microscope observation. We identified retrograde lipid transfer from the IM to the ER by measuring the recovery of R18 fluorescence at the ER–IM MCS after photobleaching. These findings indicate a reversible one-way lipid transfer mediated by Atg2 at the ER–IM MCS in response to environmental changes. Our research provides direct *in vivo* evidence of the reversible lipid transfer mediated by the bridge-like LTP Atg2, offering new insights into the dynamic regulation of lipid homeostasis during autophagy.

Results

R18 stains the ER and each autophagy-related membrane structure

R18 is a lipophilic fluorescent dye with an alkyl tail composed of 18 carbon atoms, allowing it to be easily inserted into phospholipid membranes. In the last century, it was used to stain membranes in *in vitro* assays; however, its use was gradually phased out with the development of a series of fluorescently labeled phospholipids[33, 34]. We assessed the ability of R18 to label ARSs by performing colocalization analysis using yeast cells expressing Atg8, a marker of ARSs, tagged with mNeonGreen (mNG). mNG–Atg8 was visualized as a distinct dot corresponding to the pre-autophagosomal structure/phagophore assembly site (PAS) in wild-type (WT) cells (Figure 1A and 1B). In contrast, the dot observed in *atg2*Δ cells was not labeled with R18 (Figure 1A and 1B). The Atg2–Atg18 complex is absent in the PAS of *atg2*Δ cells[23]. This suggests that the Atg2–Atg18 complex is involved in the staining of the PAS with R18. Because the IM appears as a dot in WT cells, we enlarged it into a cup-shaped structure by overexpressing prApe1, a selective autophagy cargo (see Figure 4B)[24]. We found that mNG–Atg8 labeled a cup-shaped IM and colocalized with R18 (Figure 1A), as previously reported[35]. We then used the W303 background cells to examine whether a ring-shaped autophagosome could be stained with R18[25]. We found that R18 was colocalized with ring-shaped autophagosomes (Figure 1A and 1B). These data collectively demonstrate that R18 is a fluorescent dye capable of *in vivo* labeling of IMs and autophagosomes.

The outer membrane of the autophagosome fuses with the vacuolar membrane. The inner membrane compartment, referred to as the autophagic body, is then released into the vacuolar lumen and degraded[36]. Here, we examined whether the autophagic body was labeled with R18. We found that mNG–Atg8 diffused throughout the vacuolar lumen of WT cells, representing the disintegration of autophagic bodies (Figure 1C and 1D). Conversely, the vacuolar lumen was not stained with mNG–Atg8 in *atg2*Δ cells (Figure 1C and 1D). Atg15 and Pep4 are crucial vacuolar hydrolases for the breakdown of autophagic bodies[37-40]. In *atg15*Δ and *pep4*Δ cells, the mNG–Atg8-labeled autophagic bodies were found to accumulate inside the vacuole and colocalized with R18, indicating that R18 can label autophagic bodies (Figure 1C and 1D).

ER-phagy is a type of selective autophagy in which the ER is specifically sequestered within autophagosomes and then degraded[41-43]. Because R18 also stains the ER, the dots visualized with R18 could be R18-labeled ER engulfed into autophagic bodies. We used ER-phagy-deficient cells to exclude this possibility. Atg39 and Atg40 localize to the ER membrane, where they participate in the ER-phagy-dependent degradation of the perinuclear and cortical ER, respectively[43]. The *atg39*Δ *atg40*Δ cells exhibited diffusion of mNG within the vacuole (Figure 1E and 1F), indicating that autophagosomes lacking the ER were transported into the vacuole. In *atg15*Δ or *atg15*Δ *atg39*Δ *atg40*Δ cells, we observed the accumulation of mNG-Atg8-labeled autophagic bodies inside the vacuole (Figure 1E and 1F), suggesting the inhibition of autophagic body degradation. Consistently, we found an accumulation of R18-positive

autophagic bodies in these cells (Figure 1E and 1F). These results suggest that the limiting membranes of autophagic bodies are labeled with R18. We conclude that R18 can serve as a traceable marker for the membrane dynamics of each ARS, including the IM, autophagosome, and autophagic body.

We further validated the localization of R18 by examining its colocalization with green fluorescent protein (GFP)-tagged organelle marker proteins (Figure S1A). We first used FM4-64, which can stain each compartment along the endocytosis pathway and localize to the vacuolar membrane, to validate our method (Figure S1B and S1C). Subsequently, cells expressing GFP-tagged organelle marker protein-expressing cells were stained with R18. We found that R18 colocalized with the ER membrane marker proteins Dpm1-GFP, Erd2-GFP, and Sec61-GFP, which have distinct subcellular localizations (Figure S2). R18 colocalized strongly with these ER markers (Figure S2) but failed to colocalize with other organelles (Figure S2), indicating that R18 selectively stains the ER. Additionally, R18-positive regions overlapped because ER membranes spread throughout the cytoplasm, forming contacts between organelles. These results further demonstrate that R18 preferentially stains the ER.

Finally, we confirmed whether R18 can be used in mammalian cells by testing it in mouse embryonic fibroblasts (MEFs) expressing GFP-tagged ER marker proteins. Under normal conditions, GFP and R18 exhibited clear colocalization following R18 staining (Figure 1G). After starvation-induced autophagy, we found that R18 colocalized with GFP-LC3, an autophagosome marker (Figure 1H). Cross-sectional imaging confirmed that R18 colocalized with GFP-LC3 in the XY and XZ planes, indicating the suitability of R18 for studying autophagy in mammalian cells (Figure 1H).

R18 is internalized by flippases at the plasma membrane

We investigated how R18 enters cells and stains the ER, comparing it to the internalization pathway of the well-established lipophilic dye FM4-64[44]. In contrast to FM4-64, which localizes to endocytic compartments, R18 preferentially stains the ER and ARSs (Figures. S1 and S2). These results suggest that FM4-64 and R18 are internalized and transported via different pathways. FM4-64 is internalized via endocytosis, which depends on physiological temperature and ATP[44]. Here, we examined whether biological processes also influence the internalization of R18. We expressed GFP-tagged Dpm1 as a marker of ER transmembrane proteins. At 30°C, cells displayed clear colocalization of R18 with Dpm1-GFP, which preferentially stained the ER (Figure 2A and 2B). However, at 4°C, a drastic accumulation of R18 on the PM was observed (Figure 2A and 2B), suggesting that the internalization of R18 is temperature-dependent. Next, ATP depletion was achieved by inhibiting ATP synthesis through oxidative respiration and glycolysis using NaN_3 and NaF, respectively[45]. Without these inhibitors, R18 colocalized with the ER containing Dpm1-GFP (Figure 2D and 2E). However, in the presence of these inhibitors, R18 accumulated on the PM, forming a distinct circular pattern (Figure 2D and 2E). We then washed out NaN_3 and NaF using fresh medium (Figure 2C) and found that R18 rapidly entered the cells,

colocalizing with Dpm1-GFP within 3 min (Figure 2D and 2E). This observation indicates the rapid transfer of R18 from the outside of cells to the ER. These results demonstrate that R18 internalization depends on physiological temperature and ATP.

Based on the above results, we hypothesized that flippase is involved in the internalization of R18. Flippase is a type 4 P-type ATPase (P4-ATPase) that catalyzes the translocation of phospholipids from the extracellular leaflet to the cytoplasmic leaflet[46]. Budding yeast exhibit five P4-ATPases (Drs2, Dnf1, Dnf2, Dnf3, and Neo1) that form heterodimeric complexes with noncatalytic subunits of three Cdc50 family member proteins, namely, Cdc50, Lem3, and Crf1[47, 48] (Figure 2F). Among them, Drs2, Dnf1/Dnf2, and Dnf3 form complexes with Cdc50, Lem3, and Crf1, respectively. *Neo1* is an essential gene by itself[49]. Therefore, the phenotypes observed in P4-ATPase-deficient cells should be copied to those observed in cells lacking its subunits [47, 50]. We examined R18 localization in flippase-defective cells. ER staining was defective in *drs2*Δ cells, consistent with the pattern observed in *cdc50*Δ cells, which lack the β-subunit of the P4-ATPase flippase complex. Notably, R18 staining was restricted to the PM as discrete dots (Figure 2G and 2H). Furthermore, Neo1-defective cells exhibited a distinct circular pattern, suggesting that R18 is blocked at the PM (Figure 2G and 2H). Quantification of the different patterns revealed a significant difference, suggesting that the Drs2/Cdc50 and Neo1 flippases play crucial roles in the internalization of R18 (Figure 2I).

Considering that R18 labels ARSs, we hypothesized that the absence of flippase would result in functional defects in autophagy. To test this hypothesis, we performed the GFP–Atg8 processing assay. A centromeric plasmid expressing GFP–Atg8 was transformed into the WT cells, *atg1*Δ cells (the negative control), and each flippase-deficient cell line. Samples were collected and analyzed by western blotting using GFP-specific antibodies. The significant increase in free-GFP levels in WT cells represents the normal progression of autophagy (Figure 2J and 2K). The processing of GFP–Atg8 in *lem3*Δ, *drs2*Δ, *cdc50*Δ, *dnf3*Δ, *crf1*Δ, and Neo1-defective cells was identical to that in the WT cells, indicating that the flippases are not essential for autophagy (Figure 2J and 2K).

We also investigated selective autophagic activity using the Ape1 maturation assay. In selective autophagy, the precursor Ape1 (prApe1) forms oligomers, which are transported from the cytoplasm into a vacuole and processed into mature Ape1 (mApe1)[23]. Both prApe1 and mApe1 were detected using western blotting. Each flippase-defective cell line, but not *atg1*Δ cells, exhibited processing ability comparable to WT cells (Figure 2L and 2M), suggesting that selective autophagic activity was normal in flippase-defective cells. These findings indicate that flippase does not affect autophagy.

R18 is transferred to the ER by oxysterol-binding protein (OSBP)-related proteins (ORPs) in the ER–PM MCS

We investigated how R18 translocates from the outer and inner leaflets of the PM before being transferred to the ER. FM4-64 is internalized through endocytosis in 10–15 min[44]. In contrast, our results (Figure 2D) revealed a rapid transfer of R18 from the PM to the ER in <3 min. This transfer time is consistent with the time taken for phospholipid transfer by LTPs at the PM–ER membrane contact sites[51, 52]. Furthermore, unlike FM4-64, which primarily stains the organelles in the endocytosis pathway, R18 stains only the ER and ARSs. We hypothesized that the transfer of R18 from the PM to the ER was carried out by LTPs at the PM–ER MCS.

OSBP ORPs are phospholipid transfer proteins localized to MCSs[53]. In yeast, seven homologs (Osh1–Osh7) mediate nonvesicular sterol transport at the PM–ER MCS[53]. We examined several Osh deletion cells, including *osh3*Δ, *osh1*Δ *osh2*Δ, *osh4*Δ *osh5*Δ, and *osh6*Δ *osh7*Δ. Because deletion of *OSH1-7* is lethal to cells, we used cells harboring the temperature-sensitive allele *osh4-1* in combination with deletions of the other six *OSH* genes (*osh*Δ *osh4-1*). These cells grow at the permissive temperature of 25°C but not at the nonpermissive temperature of 37°C. R18 displayed normal ER localization in WT cells, whereas no notable defects in R18 localization were observed in Osh deletion cells (Figure S3). R18 transport from the PM to the ER was partially impaired in *osh1*Δ *osh2*Δ, *osh6*Δ *osh7*Δ, and *osh*Δ *osh4-1* cells (Figure S3). These results suggest that Osh proteins participate in transferring R18 from the PM to the ER. We used orsaponin (OSW-1), a natural compound known to inhibit OSBP function[54, 55], to further validate the role of OSBP in R18 transport. Treatment with OSW-1 caused a noticeable increase in the proportion of cells exhibiting partial PM-localized R18 patterns in Osh deletion cells (Figure 3A–3C). In the temperature-sensitive *osh1-7*Δ *osh4-1* cells, R18 displayed a clear circular pattern on the PM under restrictive conditions (37°C), indicating a complete block in its transport to the ER (Figure 3A–C).

Given that R18 exhibited the same clear circular pattern in Neo1-defective cells, we hypothesized that R18 would remain on the outer leaflet of the PM in Neo1-defective cells and accumulate on the inner leaflet of the PM in OSBP-defective cells. To examine the localization of R18, we treated WT, Neo1-defective, and OSBP-defective cells with sodium dithionite to quench the fluorescence of R18 exposed to the extracellular environment (Figure 3D). We observed no discernible difference in R18 intensity in the ER of WT cells. However, compared with the stable R18 intensity at the PM of OSBP-defective cells, the R18 intensity at Neo1-defective cells decreased significantly (Figure 3E and 3F). This result indicates that R18 remained on the extracellular leaflet and was not internalized in Neo1-defective cells. In contrast, the clear circle pattern on the PM observed in OSBP-deficient cells indicates that R18 accumulates on the cytoplasmic leaflet of the PM and fails to be transferred to the ER. These findings support our hypothesis that flippase and OSBP facilitate R18 transport from the PM to the ER at the PM–ER MCS.

Phospholipids are transferred from the ER to the IM at the ER–IM MCS via Atg2

Autophagosome formation requires a constant supply of phospholipids. For several

decades, the source of the lipids essential for autophagosome formation has been a central and longstanding enigma in the field of autophagy. Previous *in vitro* studies suggested that Atg2 acts as an LTP[13-15, 26]. Moreover, Atg2 localizes between the ER and IM[24, 25]. Therefore, we hypothesized that Atg2 acts as an LTP at the ER–IM MCS (Figure 4A). To date, no direct evidence has been found to confirm lipid transfer at the ER–IM MCS in living cells, primarily due to the lack of a probe capable of monitoring phospholipid dynamics. Given that R18 stains both the ER and IM (Figure 1), we tried to use R18 as a probe to visualize phospholipid transfer from the ER to the IM *in vivo*.

The IM visualized using mNG–Atg8 appeared as a cup-shaped structure following prApe1 overexpression (Figure 4B). A recent *in silico* study has predicted an Atg2 lipid transfer mutant (*atg2*^{LT}) that the density of phospholipid in the hydrophobic cavity is discontinuous[56]. We constructed the Atg2 lipid transfer mutant. In this mutant, Ape1 maturation was not detected, showing that the process of autophagy is completely blocked, whereas full length Atg2 was expressed (Figure S4). In WT cells, R18 colocalized with mNG-Atg8 as a cup-shaped structure (Figure 4C and 4D). In contrast, *atg2*Δ cells showed a dot pattern without R18 as previously reported[35]. Furthermore, *atg2*^{LT} cells showed the same pattern with *atg2*Δ cells (Figure 4C and 4D). These results demonstrate that staining of ARSs with R18 requires the lipid transfer activity of Atg2.

We next confirmed that R18 stained the IM, as observed under a confocal microscope (Figure 4E). We then performed the fluorescence recovery after photobleaching (FRAP) assay to investigate the dynamics of lipid transfer. We performed photobleaching on both R18 and mNG signals within the expanding IM and monitored their fluorescence recovery (Figure 4F). The R18 fluorescence recovered rapidly, with a half-recovery time of 10–30 s, suggesting efficient phospholipid transfer from the ER to the IM at the ER–IM MCS (Figure 4F and 4G). Conversely, the mNG–Atg8 fluorescence did not recover (Figure 4F and 4G). These findings indicate that phospholipid transfer occurs from the ER to the IM at the ER–IM MCS. Furthermore, the length of the IM at 320 s was increased compared with that at 0 s (Figure 4F and 4H), indicating that the supply of Atg8 to the IM is not required during IM expansion.

Phospholipids are transferred from the IM to the ER after autophagy termination

Although the prApe1 overexpression system enlarged the IM, it can obstruct the formation of a complete autophagosome. Therefore, we focused on the IM when it reached its maximum length during prolonged autophagy (Figure 5A). We performed photobleaching of R18 in a large region encompassing the IM, ER–IM MCS, and adjacent ER areas and subsequently monitored the fluorescence recovery at each area (Figure 5B and 5C). The IM length did not increase after reaching the maximum length (Figure 5D). The R18 signal at the IM did not recover, indicating that phospholipid transfer from the ER to the IM had ceased (Figure 5C and 5E). We observed a normal recovery curve for R18 at the ER, showing a rapid and distinct recovery. The R18 signal at the ER–IM MCS was expected to recover at a rate

comparable to that of the R18 signal at the ER. However, the fluorescence recovery was partial (Figure 5C and 5E). This outcome indicates the possible transfer of phospholipids from the quenched IM to the ER–IM MCS, indicating a previously unrecognized retrograde phospholipid flow from the IM to the ER.

To test the possibility of phospholipid transfer from the IM to the ER, we investigated whether this transfer occurs after the termination of autophagy. Cells were subjected to starvation for 4 h in a nitrogen-starvation medium, stained with R18, and seeded onto a glass-bottom dish. Subsequently, autophagy was terminated by replenishing the cells with a nutrient-rich medium, and the cells were examined using time-lapse microscopy (Figure 5F). We then photobleached several regions (the IM / the ER with the ER-IM MCS) to examine phospholipid transfer.

To determine whether nutrient replenishment terminates autophagy, we monitored the mNG–Atg8 signal following nutrient replenishment without photobleaching. We observed a marked decrease in the mNG–Atg8 signal (Figure 5G–5I), indicating the dissociation of Atg8 from the IM. Based on this result, we conclude that nutrient repletion terminates autophagosome formation. Next, we photobleached the R18 signal on the IM 80 s after nutrient replenishment (Figure 5H). We observed minimal fluorescence recovery at the IM (Figure 5H and 5J), suggesting that phospholipid transfer from the ER to the IM ceases upon autophagy termination (Figure 5H and 5J). Therefore, the cessation of anterograde lipid transfer is likely accompanied by the termination of autophagosome formation.

Next, we photobleached the ER region and monitored R18 signal recovery at the ER–IM MCS (Figure 5J and 5K). Time-lapse imaging revealed gradual dissociation of mNG–Atg8 at the IM after autophagy termination (Figure 5K). During this period, the mNG–Atg8-labeled IM disappeared (Figure 5L). Following photobleaching in the ER region, R18 fluorescence was recovered at the ER–IM MCS (Figure 5K). To determine whether the phospholipids at the ER–IM MCS originated from the IM or ER, we generated a fluorescence intensity recovery curve at the ER–IM MCS, normalizing it to the intensity of the unbleached IM or ER region as the background. We observed a significant recovery of R18 fluorescence at the ER–IM MCS when the R18 fluorescence at the ER–IM MCS was normalized to that of the unbleached IM (Figure 5M), suggesting that a portion of the phospholipids in the ER–IM MCS were supplied from the IM following nutrient replenishment. These findings indicate that the phospholipids on the IM may be transferred back to the ER during IM shrinkage after autophagy termination. Therefore, our findings provide evidence of reversible one-way lipid transfer at the ER–IM MCS.

To gain insights into the structural properties underlying the Atg2-mediated phospholipid transfer process, we employed the predictive capabilities of AlphaFold3. We modeled a system consisting of 12 molecules of 1-palmitoyl-2-oleoyl-glycero-3-phosphocholine (POPC), 12 molecules of 1,2-dioleoyl-sn-glycero-3-

phosphoethanolamine (DOPE), four molecules of R18, and the RBG domain of Atg2 (residues 1–1346). The phospholipids and R18 molecules were aligned in a side-by-side configuration via the RBG domain of Atg2 (Figure 6A). Because of the inability to identify the mechanism governing the directionality of phospholipid transfer, this result suggests that phospholipids can diffuse in either direction. Cellular requirements may regulate the direction of phospholipid transfer at the ER–IM MCS. For instance, phospholipids are transferred from the ER to the IM via Atg2 during autophagosome formation. Conversely, upon autophagy termination, the phospholipid flow appears to be reversed, with the retrieval of phospholipids from the IM to the ER. The present study posits that the ER–IM MCS is a pivotal hub for regulating lipid flux between the IM and ER.

Discussion

The study of MCSs substantially enhanced our understanding of phospholipid transfer, revealing that nonvesicular transport processes facilitate rapid and efficient lipid exchange between organelles. These processes are critical for maintaining cellular homeostasis, especially under stress or nutrient-deprivation conditions. In particular, the recent discovery of bridge-like LTPs has further significantly advanced our understanding of the structural and functional intricacies of phospholipid transfer. Bridge-like LTPs such as Atg2 and Vps13 act as molecular conduits for lipid transport, facilitating the coordinated transfer of lipids across MCSs. Despite significant structural and biochemical research progress, our understanding of lipid dynamics in living cells remains limited. Most of our current knowledge is based on *in vitro* experiments, raising concerns about the translatability of *in vitro* findings in fundamental biological research[57].

A major constraint in our *in vivo* investigation of lipid transfer thus far has been the lack of a probe to monitor phospholipid movement. R18 was initially used to study membrane fusion during viral infection *in vitro* around 1980, coinciding with the establishment of *in vitro* assays. However, this application was subsequently abandoned by approximately 2000[34]. Our group had previously reported that R18 stains the ER[35]. The ER forms various MCSs with other organelles to facilitate lipid exchange via bridge-like LTPs. Among these LTPs, Vps13 localizes to multiple organelles and MCSs, including the ER-mitochondrion and ER-endosome MCSs[11]. But R18 specifically stained the ER, not the other organelles (Figure S1 and S2). Moreover, our findings indicate that R18 is specifically transferred via Atg2 at the ER–IM MCS (Figure 1 and 4). Therefore, the transfer of R18 mediated by Vps13 and other bridge-like LTPs may be limited. The regulation of phospholipid transfer in various MCSs may involve a gating function restricting phospholipid transfer.

Our study analyzed phospholipid transfer pathways using R18 from the external environment of cells. In comparison with existing phospholipid traceable probes, such as FM4-64, NBD-PC, and NBD-PE, which are transported via the endocytosis pathway, we have established R18 as a novel probe for tracking lipid transfer through the nonvesicular pathway in living cells. R18 was initially flipped from the outer to the inner leaflet on the PM by the flippases Neo1 and Drs2 (Figure 2). Flippases are a type of phospholipid transporter responsible for maintaining lipid asymmetry[48]. R18 exhibited a distinct circular pattern on the PM in Neo1-defective cells, in contrast to a dot pattern in Drs2 deletion cells, suggesting the presence of entry regions or tethering sites for phospholipid translocation. Neo1 is likely required for R18 to access these entry regions on the PM. However, Neo1 is an essential protein with poorly understood functions. It is believed to be involved in recycling processes at the endosome and trans-Golgi network while also playing a role in regulating the phospholipid composition of the PM[58]. Our findings provide valuable insights that could inform future mechanistic studies of Neo1. We found no direct relationship between flipping and autophagic activity, suggesting that the translocation of R18 is independent, even when it reaches

each ARS.

Following the treatment of *osh*Δ *osh4-1* cells with OSW-1, an OSBP inhibitor, at a restrictive temperature, R18 displayed a distinct circular blocking pattern (Figure 3). This result indicates the transfer of R18 from the PM to the ER via OSBP. One potential explanation for this phenomenon is that OSW-1 strongly binds to Osh4-1 at the restrictive temperature. An alternative explanation is that undetermined OSBP(s) with low activity levels may exist that are effectively inhibited by OSW-1. Further elucidation of the molecular mechanisms underlying flippase and OSBP function requires more detailed structural studies. FRAP analysis of R18 can also be performed at the PM–ER MCS to investigate phospholipid transfer *in vivo*.

We demonstrated that R18 labels ARSs in both yeast and mammalian cells (Figure 1). Because Atg9 is proposed to function as a scramblase that regulates phospholipids transferred from Atg2 at the edge of the expanding IM, both leaflets of the autophagic body membrane should be stained with R18. This suggests that R18 is useful for analyzing the Atg9 function. In mammalian cells, the IM is sandwiched between the ER membranes, making it difficult to solely identify the flow of phospholipids within the IM[16]. Therefore, we considered *Saccharomyces cerevisiae* a suitable organism for determining the directions of phospholipid transfer at the ER–IM MCS. A major point of contention in the field of autophagy is the primary phospholipid source for autophagosome formation[59]. Our *in vivo* results strongly support the ER as the main membrane source of phospholipids, which are transferred via Atg2 to the expanding IM (Figure 4).

To investigate reversible phospholipid transfer, we leveraged the inherent defect of the prApe1 overexpression system as a key tool to enlarge the IM and prevent its closure into a complete autophagosome. We developed a nutrient-rich medium replenishment assay to induce autophagy termination and focused on the IM with the maximum length (Figure 5). Our findings demonstrate both retrograde phospholipid flow from the IM to the ER and gradual dissociation of mNG–Atg8 from the IM after autophagy termination. This may lead to the disintegration of the IM, suggesting a role for Atg8 localization in IM stability. Further research employing additional marker proteins for the IM (Atg1 and Atg16-5-12) is essential to comprehensively understand the disintegration process. We also developed a phospholipid transfer model of Atg2 (residues 1–1346) using AlphaFold3[60] (Figure 6A). The side-by-side alignments in the RBG cavities further support our *in vivo* evidence for the reversible one-way lipid transfer via Atg2 at the ER–IM MCS. This finding highlights the critical role of bridge-like LTPs at MCSs in response to dynamic environmental conditions.

Our *in vivo* evidence demonstrated that reversible phospholipid transfer by Atg2 is a key mechanism by which cells regulate lipid homeostasis during autophagy induction and termination (Figs. 4–6). These findings also raise intriguing questions, such as how cells regulate millions of phospholipid molecules within minutes, transferring them

466 via bridge-like LTPs at MCSs in response to environmental changes. A major issue not
467 addressed in this study is the driving force for the reversible one-way lipid transfer at
468 the ER–IM MCS via Atg2. Based on our findings, we hypothesized that a driving force
469 acts on donor and receptor organelles. Furthermore, based on the studies of VPS13
470 in mammalian cells and the role of the Atg2–Atg9 complex in autophagy, we propose
471 that cells regulate phospholipid transfer through a gating function in response to
472 environmental changes. Bridge-like LTPs are likely regulated by other proteins, such
473 as scramblase, localized at both organelles at MCSs. Nevertheless, this study
474 successfully identified a traceable probe for phospholipids undergoing nonvesicular
475 transport and demonstrated reversible, one-way lipid transfer via Atg2 at the ER–IM
476 MCS. This major advancement contributes to our understanding of phospholipid
477 transfer via bridge-like LTPs, which play a role in various cellular functions *in vivo*.
478 Additionally, it provides insights into the chemical and biophysical aspects necessary
479 for developing traceable probes for nonvesicular transport.

Methods

Yeast strains and media

The S. cerevisiae strains and plasmids used in this study are listed in Supplementary Tables 1 and 2, respectively. Cells were cultured in YPD (1% Bacto™ yeast extract, 2% Bacto™ peptone, and 2% glucose), SDCA (0.17% Difco™ yeast nitrogen base w/o amino acids and ammonium sulfate, 0.5% ammonium sulfate, 0.5% Bacto™ casamino acids, and 2% glucose), or SDGA (0.17% Difco™ yeast nitrogen base w/o amino acids and ammonium sulfate, 0.5% ammonium sulfate, 0.5% Bacto™ casamino acids, and 2% galactose) supplemented with appropriate nutrients. Plasmid amplification was performed using *Escherichia coli* strain XL1-Blue grown in LB medium (1% Bacto™ tryptone, 0.5% Bacto™ yeast extract, and 1% NaCl). Ampicillin was added to the LB medium at 60 μg/mL when relevant. Yeast cells were transformed using the lithium acetate method[62]. The *atg2*^{LT} mutant cells are constructed by the CRISPR/Cas9 system provided by Ellis lab (https://benchling.com/pub/ellis-crispr-tools).

To activate the Cu^{2+}-inducible *CUP1* promoter, cells were cultured for 1 day in a medium containing 250 μM $CuSO_4$ prior to the experiments. Autophagy was induced by transferring cells to nitrogen-starvation SD(−N) medium (0.17% yeast nitrogen base without amino acids and ammonium sulfate, and 2% glucose) or by treating cells with 0.2 μg/mL rapamycin (Sigma Aldrich). Standard protocols were used for yeast manipulation[61].

The yeast cells were treated with a mixture of NaF and NaN_3 at a final concentration of 10 mM for 5 min. For galactose induction of *Neo1* using the *GAL1* promoter, cells were cultured in SDGA medium supplemented with appropriate nutrients. The following day, the cells were collected and washed three times with an SDCA medium to remove the galactose, initiating the suppression of *Neo1* expression. The cells (OD_{600} = 1.0–2.0) were then resuspended in SDCA medium and incubated for 12 h to suppress *Neo1* expression.

Fluorescence microscopy

Cells were cultured overnight, diluted, and then cultured in SDCA medium supplemented with appropriate nutrients until reaching the log phase (~2 × 10^7 cells per mL; OD_{600} = ~1). For R18 staining, cells were incubated with R18 (Invitrogen) at 5 μg/mL (from a 1 mg/mL stock dissolved in dimethyl sulfoxide) for 10 min in a nutrient-rich medium at 30℃. The cells were then washed thrice with a fresh medium. FM4-64 staining was performed as previously described[44].

For visualization of IM, cells were cultured in the presence of 250 μM $CuSO_4$ overnight to activate the *CUP1* promoter and induce prApe1 expression. The cells were then diluted and cultured in SDCA medium containing 250 μM $CuSO_4$ until they reached the log phase (~2 × 10^7 cells per mL; OD_{600} = ~1). Fluorescence imaging was performed using an IX83 inverted system microscope (Olympus) equipped with a UPlanSApo100× oil-immersion lens (1.40 NA; Olympus) and a CoolSNAP HQ CCD camera (Nippon Roper). U-HGLGPS (Olympus), a mercury light source system, was used to excite fluorescent proteins. U-FGFP and U-FRFP filter sets (Olympus) were

524 used for GFP and R18 visualization, respectively. Images were acquired using the
525 Micro-Manager software (version 1.4.6, https://micro-manager. org). Samples were
526 prepared on 76×26-mm glass slides (S1225; Matsunami) and 18×18-mm glass
527 coverslips (No. 1-S; Matsunami).
528
529 **Confocal microscopic analysis of mammalian cells**
530 ER (Calreticulin-KDEL-GFP) labeling was performed using CellLight™ ER-GFP,
531 BacMam 2.0 (C10590; Thermo Fisher Scientific). To induce autophagy, MEFs stably
532 expressing GFP-LC3 were cultured in Earle's Balanced Salts (E2888-500ML; Sigma)
533 for 3 h.
534 Live cells seeded in 35-mm glass-bottom dishes (P35G-1.5-14-C; Mattek) were
535 maintained at 37 °C with 5% CO_2 and observed under a Ti2 inverted microscope (Nikon)
536 equipped with a Nikon A1 HD25 (Nikon) confocal system and Plan Apo λ 60x oil-
537 immersion lens (1.4 NA; Nikon). The pinhole size was set to 1.0 Airy units. For 3D
538 imaging, z-stack images were acquired using a Plan Apo λ 60x oil-immersion lens with
539 Galvano scanning using two frame averages, and the pinhole size was set to 0.8 Airy
540 units. The images were captured using NIS-Elements (Nikon). The images of
541 deconvolution were processed using Nikon's original ER deconvolution algorithm.
542
543 **Confocal microscopic analysis of yeast cells**
544 A confocal laser scanning microscope FV-3000 (Olympus) equipped with a
545 UPLSAPO60XO oil-immersion objective lens (1.42 NA; Olympus) was used. Lasers
546 (488 and 561 nm) were employed for linear sequential excitation, and fluorescence in
547 the ranges of 500–540 nm and 560–600 nm was recorded for mNG and octadecyl
548 rhodamine B (R18; Invitrogen), respectively, using a resonant scanner. Samples were
549 prepared on 76×26-mm glass slides (S1225; Matsunami) and 18×18-mm glass
550 coverslips (No. 1-S; Matsunami). The images were analyzed using ImageJ
551 (https://fiji.sc/).
552
553 **Quenching assay**
554 Yeast cells immobilized on concanavalin A-coated glass-bottom dishes (Mattek) were
555 imaged. They were then treated with 500 μL of 1M sodium dithionite dissolved in SDCA
556 medium while being imaged under a microscope.
557
558 **SDS–PAGE and western blotting**
559 Cells cultured in SDCA medium (2×10^7 cells per mL) were subjected to lysis using
560 alkaline trichloroacetic acid, followed by SDS–PAGE and western blotting[63]. To analyze
561 Ape1 maturation, expression of Atg2, and GFP–Atg8 processing, SDS–PAGE was
562 performed using 10% acrylamide gels. Proteins were transferred to polyvinylidene
563 fluoride membranes (Immobilon-P; Millipore) using a semi-dry transfer apparatus
564 (Trans-Blot Turbo Transfer System; Bio-Rad) at 2.5 A and 25 V for 15 min. Following
565 the transfer, the membranes were incubated with 2% skim milk in Tris-buffered saline
566 containing 0.05% Tween 20 (TBST) for 30 min at room temperature to block
567 nonspecific binding. The membranes were incubated with primary anti-Ape1

(1:10,000), anti-Atg 2 (1:5000), and anti-GFP (1:5000) antibodies for 60 min at room temperature. The membranes were washed thrice with TBST and treated with horseradish peroxidase-labeled anti-rabbit secondary antibody (Promega) at a dilution of 1:5000 for 30 min, followed by an additional wash in TBST. Chemiluminescent signals were generated using an enhanced chemiluminescence reagent (GE Healthcare) and ImmunoStar LD (Fujifilm) then detected using an IR-LAS 1000 imaging system (Fujifilm).

FRAP measurements and analysis

For the FRAP experiments assessing the IM, cells treated with rapamycin or SDCA-N were seeded onto concanavalin A-coated glass-bottom dishes (Mattek) that immobilized the cells. The experiments were performed using a confocal laser scanning microscope FV-3000 (Olympus) equipped with a UPLSAPO60XO oil-immersion objective lens (1.42 NA; Olympus). For mNG and R18 fluorescence imaging, excitation was performed using a 488 nm laser, and fluorescence was recorded at 561 nm in a linear sequential mode. Photobleaching was performed using 488 and 561 nm laser pulses. The images were analyzed using FIJI v.1.52e31. For the kinetic analysis, the relative fluorescence intensity was plotted against time, with the intensity before quenching set to 1.0 and the minimum intensity after quenching to 0.0. The data were then fitted to an exponential recovery curve: $F = A_0(1 - exp(k_{off}t))$, where t represents time in seconds, and A_0 is the maximum recovery at t = infinity.

Repletion assay using nutrient-rich medium

The cells were grown to the mid-log phase and then shifted to SDCA-N medium (0.17% Difco™ yeast nitrogen base w/o amino acids and ammonium sulfate, 0.5% Bacto™ casamino acids, and 2% glucose) to induce autophagy. The cells were then seeded on concanavalin A-coated glass-bottom dishes (Mattek) to immobilize them and were imaged. Prior to photobleaching, 1 mL of SDCA was added to the glass-bottom dish to terminate autophagy. Photobleaching and time-lapse imaging were then performed.

Statistical analysis

The statistical analyses of all experiments were performed using GraphPad Prism software (version 9.5.1).

Acknowledgments

We thank Drs. Christopher. T. Beh, Hitoshi Nakatogawa, Jasper Rine, Ryouichi Fukuda, Kishimoto Takuma, and Kazuma Tanaka for providing plasmids and strains; Dr. Kyoka Sasaki for technical support; Dr. Yoshikazu Ohya for critical advice. This work was supported in part by JSPS KAKENHI Grant Numbers JP19H05707, JP23K20044, JP23K06667, JP24H00060 (to N.N.N.), JP 20H05313, JP22H02569 (to K.S.), and CREST, Japan Science and Technology Agency Grant number JPMJCR20E3 (to K.S., N.N.N.).

610 **Author contributions**

611 K.S. supervised the project. L.H. and K.S. conceptualized the study and designed the
612 experiments. L.H. performed the experiments and data analysis. T.M. initially
613 visualized the colocalization of R18 and ARSs in yeast cells, and L.H. reproduced and
614 validated these findings. Y.O., Y.H., and N.N.N. imaged the R18 distribution in
615 mammalian cells. H.L. provided insights into R18 transport by Osh proteins, and L.H.
616 investigated it. L.H. wrote the original manuscript. L.H. and K.S. revised the manuscript.

617 **Declaration of interests**

618 The authors declare no competition of interests.

References

1. Palade, P. Intracellular Aspects of the Process of Protein Synthesis. *Science* **189**, 347–358 (1975).

2. Acoba, M. G., Senoo, N. & Claypool, S. M. Phospholipid ebb and flow makes mitochondria go. *Journal of Cell Biology* **219**, e202003131 (2020).

3. Wirtz, K. W. A. & Zilversmit, D. B. Exchange of Phospholipids between Liver Mitochondria and Microsomes in Vitro. *Journal of Biological Chemistry* **243**, 3596–3602 (1968).

4. Reinisch, K. M. & Prinz, W. A. Mechanisms of nonvesicular lipid transport. *J Cell Biol* **220**, e202012058 (2021).

5. Prinz, W. A., Toulmay, A. & Balla, T. The functional universe of membrane contact sites. *Nat Rev Mol Cell Biol* **21**, 7–24 (2020).

6. Saheki, Y. & De Camilli, P. Endoplasmic Reticulum-Plasma Membrane Contact Sites. *Annu Rev Biochem* **86**, 659–684 (2017).

7. Wong, L. H., Gatta, A. T. & Levine, T. P. Lipid transfer proteins: the lipid commute via shuttles, bridges and tubes. *Nat Rev Mol Cell Biol* **20**, 85–101 (2019).

8. Neuman, S. D., Levine, T. P. & Bashirullah, A. A novel superfamily of bridge-like lipid transfer proteins. *Trends in Cell Biology* **32**, 962–974 (2022).

9. Hanna, M., Guillén-Samander, A. & Camilli, P. D. RBG Motif Bridge-Like Lipid Transport Proteins: Structure, Functions, and Open Questions. *Annual Review of Cell and Developmental Biology* **39**, 409–434 (2023).

10. Toulmay, A. *et al*. Vps13-like proteins provide phosphatidylethanolamine for GPI anchor synthesis in the ER. *Journal of Cell Biology* **221**, e202111095 (2022).

11. Levine, T. P. Sequence Analysis and Structural Predictions of Lipid Transfer Bridges in the Repeating Beta Groove (RBG) Superfamily Reveal Past and Present Domain Variations Affecting Form, Function and Interactions of VPS13, ATG2, SHIP164, Hobbit and Tweek. *Contact (Thousand Oaks)* **5**, 251525642211343 (2022).

12. Braschi, B., Bruford, E. A., Cavanagh, A. T., Neuman, S. D. & Bashirullah, A. The bridge-like lipid transfer protein (BLTP) gene group: introducing new nomenclature based on structural homology indicating shared function. *Human Genomics* **16**, 66 (2022).

651 13. Chowdhury, S. *et al*. Insights into autophagosome biogenesis from structural and
652 biochemical analyses of the ATG2A-WIPI4 complex. *Proceedings of the National*
653 *Academy of Sciences* **115**, E9792–E9801 (2018).

654 14. Valverde, D. P. *et al*. ATG2 transports lipids to promote autophagosome
655 biogenesis. *J. Cell Biol.* **218**, 1787–1798 (2019).

656 15. Maeda, S., Otomo, C. & Otomo, T. The autophagic membrane tether ATG2A
657 transfers lipids between membranes. *Elife* **8**, e45777 (2019).

658 16. Mizushima, N., Yoshimori, T. & Ohsumi, Y. The Role of Atg Proteins in
659 Autophagosome Formation. *Annu. Rev. Cell Dev. Biol.* **27**, 107–132 (2011).

660 17. Kim, J., Huang, W., Stromhaug, P. E. & Klionsky, D. J. Convergence of Multiple
661 Autophagy and Cytoplasm to Vacuole Targeting Components to a Perivacuolar
662 Membrane Compartment Prior tode Novo Vesicle Formation*. *J. Biol. Chem.* **277**,
663 763–773 (2002).

664 18. Suzuki, K. *et al*. The pre-autophagosomal structure organized by concerted
665 functions of APG genes is essential for autophagosome formation. *EMBO J* **20**,
666 5971–5981 (2001).

667 19. Wang, Z. & Zhang, H. Phase Separation, Transition, and Autophagic Degradation
668 of Proteins in Development and Pathogenesis. *Trends Cell Biol.* **29**, 417–427 (2019).

669 20. Reggiori, F., Tucker, K. A., Stromhaug, P. E. & Klionsky, D. J. The Atg1-Atg13
670 complex regulates Atg9 and Atg23 retrieval transport from the pre-autophagosomal
671 structure. *Developmental cell* **6**, 79–90 (2004).

672 21. Obara, K., Noda, T., Niimi, K. & Ohsumi, Y. Transport of phosphatidylinositol 3-
673 phosphate into the vacuole via autophagic membranes in Saccharomyces cerevisiae.
674 *Genes to Cells* **13**, 537–547 (2008).

675 22. Gómez-Sánchez, R. *et al*. Atg9 establishes Atg2-dependent contact sites
676 between the endoplasmic reticulum and phagophores. *J. Cell Biol.* **217**, 2743–2763
677 (2018).

678 23. Suzuki, K., Kubota, Y., Sekito, T. & Ohsumi, Y. Hierarchy of Atg proteins in pre-
679 autophagosomal structure organization. *Genes to Cells* **12**, 209–218 (2007).

680 24. Suzuki, K., Akioka, M., Kondo-Kakuta, C., Yamamoto, H. & Ohsumi, Y. Fine
681 mapping of autophagy-related proteins during autophagosome formation in
682 Saccharomyces cerevisiae. *J. Cell. Sci.* **126**, 2534–2544 (2013).

683 25. Graef, M., Friedman, J. R., Graham, C., Babu, M. & Nunnari, J. ER exit sites are
684 physical and functional core autophagosome biogenesis components. *Mol. Biol. Cell*
685 **24**, 2918–2931 (2013).

686 26. Osawa, T. *et al*. Atg2 mediates direct lipid transfer between membranes for
687 autophagosome formation. *Nat Struct Mol Biol* **26**, 281–288 (2019).

688 27. Hailey, D. W. *et al*. Mitochondria supply membranes for autophagosome
689 biogenesis during starvation. *Cell* **141**, 656–667 (2010).

690 28. Axe, E. L. *et al*. Autophagosome formation from membrane compartments
691 enriched in phosphatidylinositol 3-phosphate and dynamically connected to the
692 endoplasmic reticulum. *J. Cell Biol.* **182**, 685–701 (2008).

693 29. Puri, C. *et al*. The RAB11A-positive compartment is a primary platform for
694 autophagosome assembly mediated by WIPI2 recognition of PI3P-RAB11A.
695 *Developmental cell* **45**, 114–131. e8 (2018).

696 30. Ge, L. *et al*. Remodeling of ER-exit sites initiates a membrane supply pathway for
697 autophagosome biogenesis. *EMBO Rep.* **18**, 1586–1603 (2017).

698 31. van Vliet, A. R. *et al*. ATG9A and ATG2A form a heteromeric complex essential
699 for autophagosome formation. *Mol. Cell* **82**, 4324–4339. e8 (2022).

700 32. Maeda, S. *et al*. Structure, lipid scrambling activity and role in autophagosome
701 formation of ATG9A. *Nature structural & molecular biology* **27**, 1194–1201 (2020).

702 33. Hoekstra, D., Klappe, K., Hoff, H. & Nir, S. Mechanism of Fusion of Sendai Virus:
703 Role of Hydrophobic Interactions and Mobility Constraints of Viral Membrane
704 Proteins: Effects of Polyethylene Glycol. *Journal of Biological Chemistry* **264**, 6786–
705 6792 (1989).

706 34. Hoekstra, D., De Boer, T., Klappe, K. & Wilschut, J. Fluorescence method for
707 measuring the kinetics of fusion between biological membranes. *Biochemistry (N.*
708 *Y.)* **23**, 5675–5681 (1984).

709 35. Hirata, E., Ohya, Y. & Suzuki, K. Atg4 plays an important role in efficient
710 expansion of autophagic isolation membranes by cleaving lipidated Atg8 in
711 Saccharomyces cerevisiae. *PLoS One* **12**, e0181047 (2017).

712 36. Baba, M., Takeshige, K., Baba, N. & Ohsumi, Y. Ultrastructural analysis of the
713 autophagic process in yeast: detection of autophagosomes and their
714 characterization. *J. Cell Biol.* **124**, 903–913 (1994).

715 37. Hirata, E. *et al*. Atg15 in Saccharomyces cerevisiae consists of two functionally
716 distinct domains. *Mol. Biol. Cell* **32**, 645–663 (2021).

717 38. Teter, S. A. *et al*. Degradation of lipid vesicles in the yeast vacuole requires
718 function of Cvt17, a putative lipase. *J. Biol. Chem.* **276**, 2083–2087 (2001).

719 39. Epple, U. D., Eskelinen, E. & Thumm, M. Intravacuolar membrane lysis in
720 Saccharomyces cerevisiae: Does vacuolar targeting of Cvt17/Aut5p affect its
721 function? *J. Biol. Chem.* **278**, 7810–7821 (2003).

722 40. Watanabe, Y. *et al*. Atg15 is a vacuolar phospholipase that disintegrates
723 organelle membranes. *Cell Reports* **42** (2023).

724 41. Bernales, S., Schuck, S. & Walter, P. ER-phagy: selective autophagy of the
725 endoplasmic reticulum. *Autophagy* **3**, 285–287 (2007).

726 42. Hamasaki, M., Noda, T., Baba, M. & Ohsumi, Y. Starvation triggers the delivery
727 of the endoplasmic reticulum to the vacuole via autophagy in yeast. *Traffic* **6**, 56–65
728 (2005).

729 43. Mochida, K. *et al*. Receptor-mediated selective autophagy degrades the
730 endoplasmic reticulum and the nucleus. *Nature* **522**, 359–362 (2015).

731 44. Vida, T. A. & Emr, S. D. A new vital stain for visualizing vacuolar membrane
732 dynamics and endocytosis in yeast. *J. Cell Biol.* **128**, 779–792 (1995).

733 45. Zhu, L., Jorgensen, J. R., Li, M., Chuang, Y. & Emr, S. D. ESCRTs function
734 directly on the lysosome membrane to downregulate ubiquitinated lysosomal
735 membrane proteins. *Elife* **6**, e26403 (2017).

736 46. Seigneuret, M. & Devaux, P. F. ATP-dependent asymmetric distribution of spin-
737 labeled phospholipids in the erythrocyte membrane: relation to shape changes.
738 *Proceedings of the National Academy of Sciences* **81**, 3751–3755 (1984).

739 47. Saito, K. *et al*. Cdc50p, a protein required for polarized growth, associates with
740 the Drs2p P-type ATPase implicated in phospholipid translocation in Saccharomyces
741 cerevisiae. *Mol. Biol. Cell* **15**, 3418–3432 (2004).

742 48. Tanaka, K., Fujimura-Kamada, K. & Yamamoto, T. Functions of phospholipid
743 flippases. *The journal of biochemistry* **149**, 131–143 (2011).

744 49. Hua, Z., Fatheddin, P. & Graham, T. R. An essential subfamily of Drs2p-related
745 P-type ATPases is required for protein trafficking between Golgi complex and
746 endosomal/vacuolar system. *Mol. Biol. Cell* **13**, 3162–3177 (2002).

747 50. Furuta, N., Fujimura-Kamada, K., Saito, K., Yamamoto, T. & Tanaka, K.
748 Endocytic recycling in yeast is regulated by putative phospholipid translocases and
749 the Ypt31p/32p–Rcy1p pathway. *Mol. Biol. Cell* **18**, 295–312 (2007).

750 51. Lev, S. Non-vesicular lipid transport by lipid-transfer proteins and beyond. *Nature*
751 *reviews Molecular cell biology* **11**, 739–750 (2010).

752 52. Stefan, C. J. *et al*. Osh proteins regulate phosphoinositide metabolism at ER-
753 plasma membrane contact sites. *Cell* **144**, 389–401 (2011).

754 53. Kentala, H., Weber-Boyvat, M. & Olkkonen, V. M. in *International Review of Cell*
755 *and Molecular Biology* (ed Jeon, K. W.) 299–340 (Academic Press, 2016).

756 54. Albulescu, L. *et al*. Broad-range inhibition of enterovirus replication by OSW-1, a
757 natural compound targeting OSBP. *Antiviral Res* **117**, 110–114 (2015).

758 55. Burgett, A. W. G. *et al*. Natural products reveal cancer cell dependence on
759 oxysterol-binding proteins. *Nat Chem Biol* **7**, 639–647 (2011).

760 56. Srinivasan, S., Álvarez, D., John Peter, A. T. & Vanni, S. Unbiased MD
761 simulations identify lipid binding sites in lipid transfer proteins. *J. Cell Biol.* **223**,
762 e202312055 (2024).

763 57. Stachowiak, J. C. & Kirchhausen, T. The beauty of simplicity in membrane
764 biology. *Nat. Cell Biol.*, 1–4 (2022).

765 58. Takar, M., Wu, Y. & Graham, T. R. The essential Neo1 protein from budding
766 yeast plays a role in establishing aminophospholipid asymmetry of the plasma
767 membrane. *J. Biol. Chem.* **291**, 15727–15739 (2016).

768 59. Nakatogawa, H., Suzuki, K., Kamada, Y. & Ohsumi, Y. Dynamics and diversity in
769 autophagy mechanisms: lessons from yeast. *Nature reviews Molecular cell biology*
770 **10**, 458–467 (2009).

771 60. Abramson, J. *et al*. Accurate structure prediction of biomolecular interactions with
772 AlphaFold 3. *Nature* **630**, 493–500 (2024).

773 61. Kaiser, C., Michaelis, S. & Mitchell, A. in *Methods in yeast genetics* (Cold Spring
774 Harbor Laboratory Press Cold Spring Harbor, NY, 1994).

775 62. Gietz, R. D. & Woods, R. A. Transformation of yeast by lithium acetate/single-
776 stranded carrier DNA/polyethylene glycol method. *Methods Enzymol* **350**, 87–96
777 (2002).

778 63. Horvath, A. & Riezman, H. Rapid protein extraction from Saccharomyces
779 cerevisiae. *Yeast* **10**, 1305–1310 (1994).

Figure

Figure 1

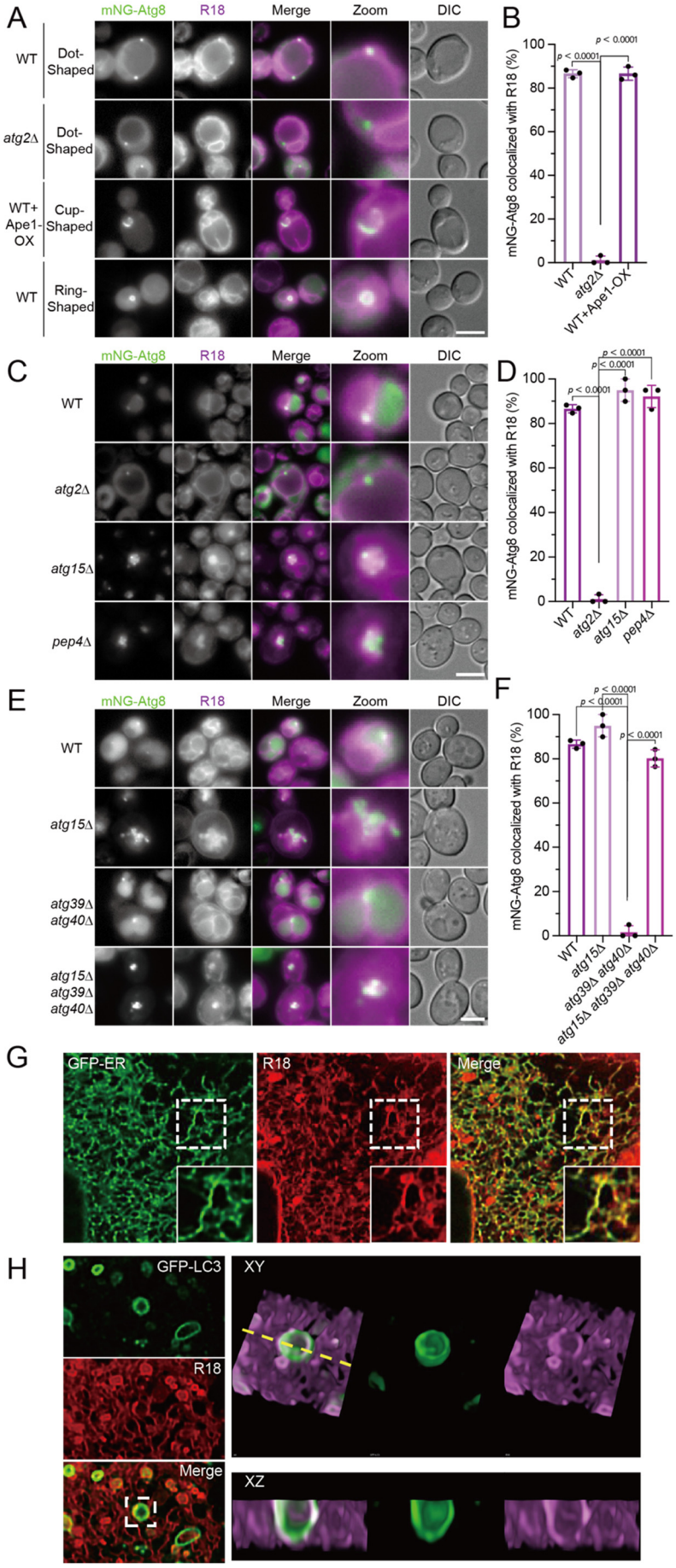

Figure 1 Octadecyl rhodamine B (R18) stains autophagy-related membrane structures.

(A) Colocalization between mNG–Atg8 and R18 in W303 background cells treated with rapamycin to induce autophagy. The scale bar represents 5 μm. WT, wild-type. OX, overexpression. mNG, mNeonGreen. DIC, differential interference contrast.

(B) Percentage of colocalization calculated using 100 cells from 3 independent experiments in (A). Error bars represent standard deviation (SD). P-values were calculated using two-way ANOVA.

(C) Colocalization between mNG–Atg8 and R18 in SEY6210 background cells. The scale bar represents 5 μm.

(D) Percentage of colocalization calculated using 100 cells from 3 independent experiments in (C). Error bars represent SD. P-values were calculated using two-way ANOVA.

(E) Colocalization between mNG–Atg8 and R18 in SEY6210 background cells. The scale bar represents 5 μm.

(F) Percentage of colocalization calculated using 100 cells from 3 independent experiments in (E). Error bars represent SD. P-values were calculated using two-way ANOVA.

(G) MEFs expressing GFP–ER were stained with R18 for colocalization analysis. The boxed area represents a higher magnification.

(H) MEFs expressing GFP–LC3 were subjected to autophagy induction by starvation and stained with R18 for colocalization analysis. The boxed area represents a higher magnification.

Figure 2

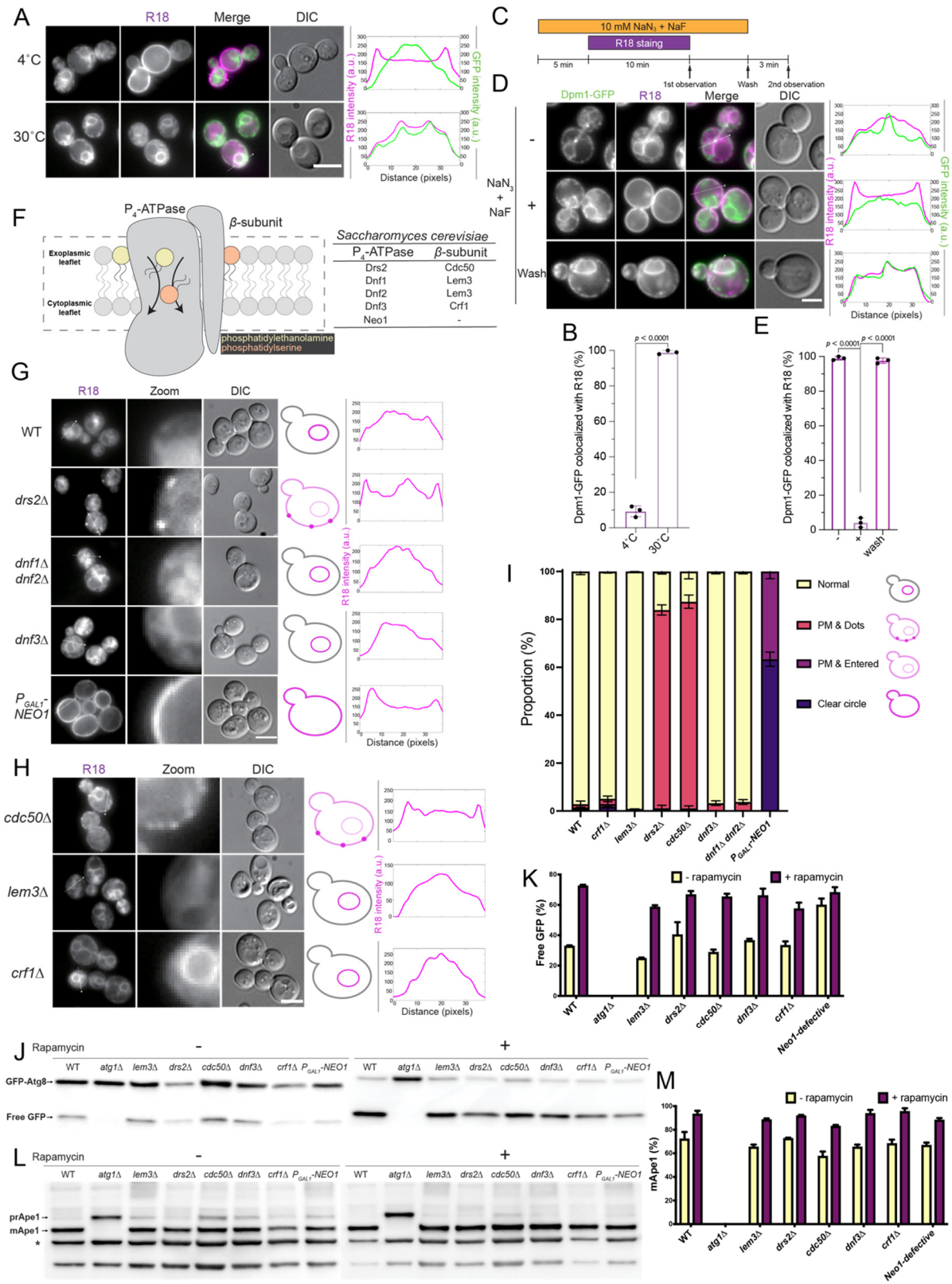
A
R18
Merge
DIC
4˚C
30˚C
R18 intensity (a.u.)
GFP intensity (a.u.)
Distance (pixels)
C
10 mM NaN3 + NaF
R18 staing
5 min
10 min
3 min
1st observation
Wash
2nd observation
D
Dpm1-GFP
R18
Merge
DIC
NaN3 + NaF
Wash
B
Dpm1-GFP colocalized with R18 (%)
p < 0.0001
4˚C
30˚C
E
wash
F
P4-ATPase
β-subunit
Exoplasmic leaflet
Cytoplasmic leaflet
phosphatidylethanolamine
phosphatidylserine
Saccharomyces cerevisiae
P4-ATPase
β-subunit
Drs2
Cdc50
Dnf1
Lem3
Dnf2
Lem3
Dnf3
Crf1
Neo1
G
R18
Zoom
DIC
WT
drs2Δ
dnf1Δ dnf2Δ
dnf3Δ
PGAL1-NEO1
H
cdc50Δ
lem3Δ
crf1Δ
I
Proportion (%)
Normal
PM & Dots
PM & Entered
Clear circle
WT
crf1Δ
lem3Δ
drs2Δ
cdc50Δ
dnf3Δ
dnf1Δ dnf2Δ
PGAL1-NEO1
K
Free GFP (%)
- rapamycin
+ rapamycin
Neo1-defective
J
Rapamycin
GFP-Atg8
Free GFP
atg1Δ
L
prApe1
mApe1
M
mApe1 (%)

Figure 2 R18 is internalized by flippases at the plasma membrane

(A) Colocalization between Dpm1–GFP and R18 in WT cells. The cells were stained with R18 at the indicated temperature. The scale bar represents 5 μm. Graphs represent the line profiles of the fluorescence intensity from the images on the left.

(B) Percentage of colocalization calculated using 100 cells from 3 independent experiments in (A). Error bars represent SD. P-values were calculated using an unpaired t-test.

(C) Illustration of the imaging process in (D). Cells were treated with NaN_3 and NaF for 5 min and then with R18 for 10 min while incubating with ATP inhibitors for the first observation. After removing NaN_3 and NaF after a 3-min wash, the cells were observed again.

(D) Colocalization between Dpm1–GFP and R18 in WT cells treated with/without NaN_3 and NaF, followed by washing out the inhibitors. The scale bar represents 5 μm. Graphs indicate the line profiles of the fluorescence intensity from the images on the left.

(E) Percentage of colocalization calculated using 100 cells from 3 independent experiments in (D). Error bars represent SD. P-values were calculated using an unpaired t-test.

(F) Model of the P4-ATPase flippase. The ATPase forms a functional complex with the β-subunit to translocate phosphatidylserine (PS) and phosphatidylethanolamine (PE) from the exoplasmic to the cytoplasmic leaflet. There are five types of flippases, and their subunits in *S. cerevisiae* are listed.

(G) R18 distribution in flippase-defective cells. *drs2*Δ cells exhibit a dot pattern (marked by arrows in the image), *dnf1*Δ *dnf2*Δ and *dnf3*Δ cells exhibit an ER pattern, and the suppression of Neo1 shows a clear circle pattern. The scale bar represents 5 μm. The phenotypes of the yeast cells representing each pattern are illustrated to the right. Graphs indicate the line profiles of the fluorescence intensity in the images on the left.

(H) R18 distribution in β-subunit deletion cells. *cdc50*Δ cells exhibit a dot pattern (marked by arrows in the image) that phenocopies the pattern observed in *drs2*Δ cells. *lem3*Δ and *crf1*Δ cells exhibit an ER pattern that phenocopies the pattern observed in *dnf1*Δ *dnf2*Δ and *dnf3*Δ cells. The phenotypes of the yeast cells representing each pattern are illustrated to the right. The scale bar represents 5 μm. Graphs indicate the line profiles of the fluorescence intensity in the images on the left.

(I) Graph representing the proportion (average ± SD) of cells with different patterns. n > 100 cells in 3 independent experiments.

(J) Autophagic activity of flippase-defective cells measured using the GFP–Atg8 processing assay. WT and flippase-defective cells carrying a GFP–Atg8 plasmid were treated with 200 ng/mL rapamycin for 2 h to induce autophagy. Western blot analysis was performed using anti-GFP antibodies. The upper bands represent GFP-tagged Atg8 (GFP-Atg8), and the lower bands represent cleaved GFP (free GFP).

(K) Quantification of the free-GFP / GFP–Atg8 ratio (mean ± SD).

846 (L) The same samples are used in (J). Western blot analysis was performed using an
847 anti-Ape1 antibody. The upper bands represent precursor Ape1 (prApe1), the middle
848 bands represent mature Ape1 (mApe1), and the lower bands represent nonspecific
849 signals that can be used as an internal control (*).
850 (M) Quantification of the mApe1/total Ape1 ratio (mean ± SD).

Figure 3

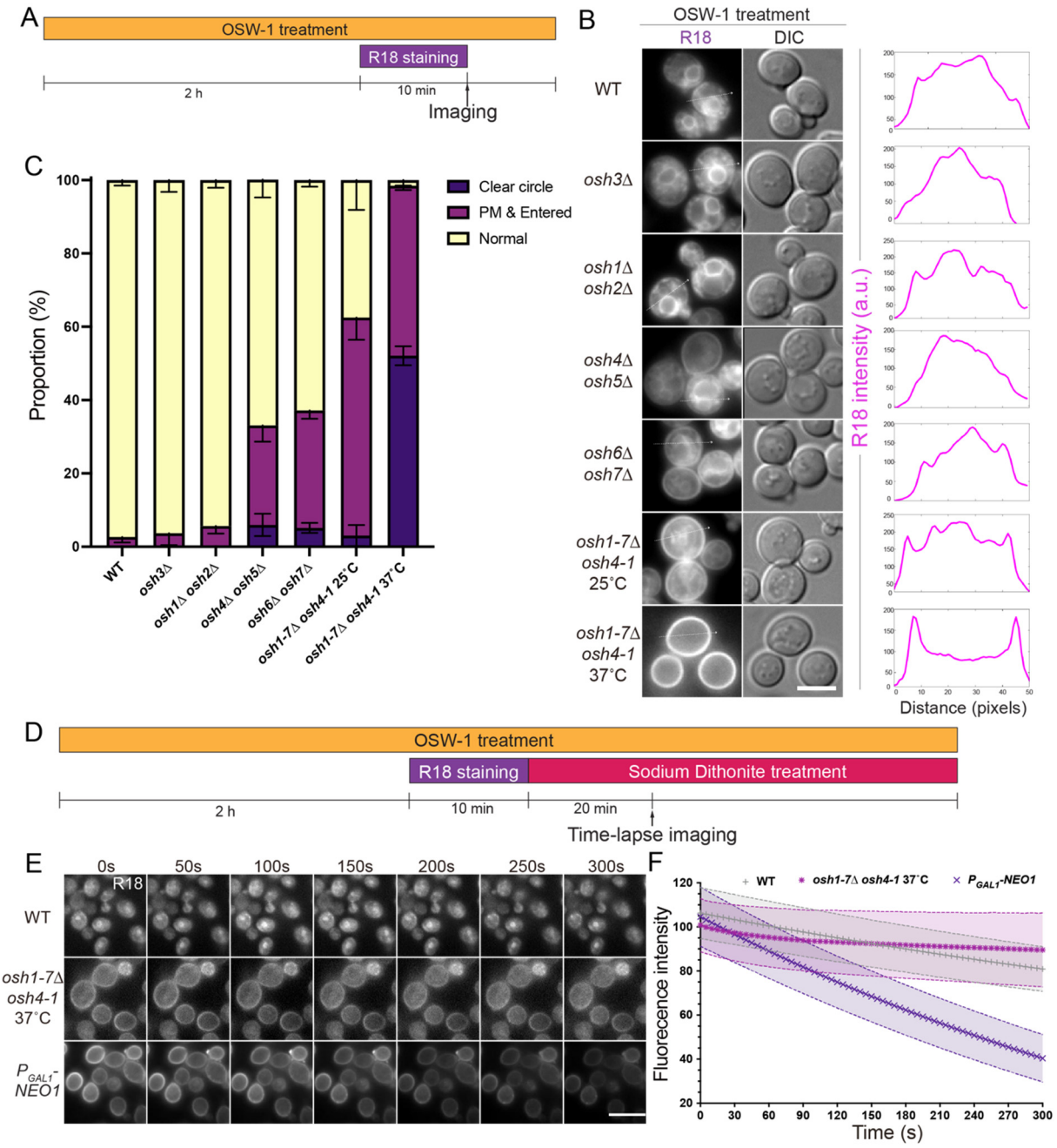
A
OSW-1 treatment
R18 staining
2 h
10 min
Imaging
B
OSW-1 treatment
R18
DIC
WT
osh3Δ
osh1Δ osh2Δ
osh4Δ osh5Δ
osh6Δ osh7Δ
osh1-7Δ osh4-1 25˚C
osh1-7Δ osh4-1 37˚C
R18 intensity (a.u.)
Distance (pixels)
C
Proportion (%)
Clear circle
PM & Entered
Normal
WT
osh3Δ
osh1Δ osh2Δ
osh4Δ osh5Δ
osh6Δ osh7Δ
osh1-7Δ osh4-1 25˚C
osh1-7Δ osh4-1 37˚C
D
OSW-1 treatment
R18 staining
Sodium Dithonite treatment
2 h
10 min
20 min
Time-lapse imaging
E
0s
50s
100s
150s
200s
250s
300s
R18
WT
osh1-7Δ osh4-1 37˚C
P GAL1-NEO1
F
WT
osh1-7Δ osh4-1 37˚C
P GAL1-NEO1
Fluorescence intensity
Time (s)

851 **Figure 3 R18 is transferred to the ER by oxysterol-binding protein (OSBP)-**
852 **related proteins (ORPs) at the ER–PM MCS**
853 (A) The procedure for the experiment in (B). Cells were stained with R18 in the
854 presence of 10 μM OSW-1.
855 (B) R18 distribution in WT and Osh deletion cells. Graphs indicate the line profiles of
856 the fluorescence intensity in the images on the left. The scale bar represents 5 μm.
857 (C) Graph representing the proportion (average ± SD) of cells with different patterns.
858 n > 100 cells in 3 independent experiments.
859 (D) The procedure for the experiment in (E). Cells were stained with R18 in the
860 presence of 10 μM OSW-1. Imaging was started 20 min after the sodium dithionite
861 treatment.
862 (E) Time-lapse imaging of WT, Osh deletion, and Neo1-suppressive cells. The scale
863 bar represents 10 μm.
864 (F) Fluorescence intensity of R18 during the time-lapse imaging in (E). Error bars
865 represent SD; n = 7.

Figure 4

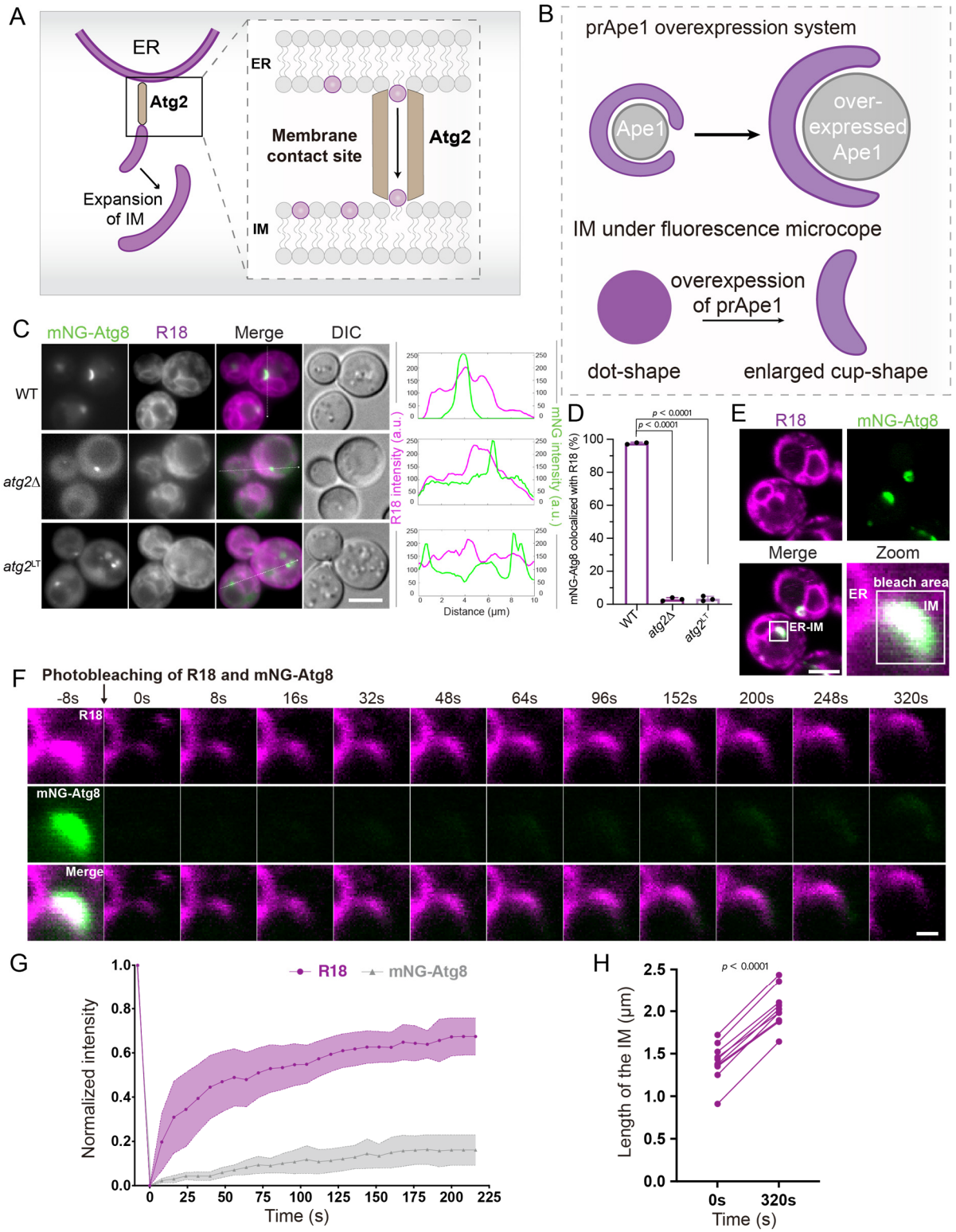
A
ER
Atg2
Expansion of IM
ER
Membrane contact site
Atg2
IM
B
prApe1 overexpression system
Ape1
over-expressed Ape1
IM under fluorescence microcope
overexpression of prApe1
dot-shape
enlarged cup-shape
C
mNG-Atg8
R18
Merge
DIC
WT
atg2Δ
atg2LT
R18 intensity (a.u.)
mNG intensity (a.u.)
Distance (μm)
D
p < 0.0001
p < 0.0001
mNG-Atg8 colocalized with R18 (%)
WT
atg2Δ
atg2LT
E
R18
mNG-Atg8
Merge
Zoom
ER-IM
ER
bleach area
IM
F
Photobleaching of R18 and mNG-Atg8
-8s
0s
8s
16s
32s
48s
64s
96s
152s
200s
248s
320s
R18
mNG-Atg8
Merge
G
R18
mNG-Atg8
Normalized intensity
Time (s)
H
p < 0.0001
Length of the IM (μm)
0s
320s
Time (s)

866 **Figure 4 Phospholipids are transferred from the ER to the IM at the ER–IM MCS**
867 **via Atg2.**
868 (A) Model of lipid transfer activity from the ER to the IM via Atg2 at the ER–IM MCS.
869 (B) Visualization of the IM as a cup-shaped structure induced by prApe1
870 overexpression.
871 (C) Colocalization between mNG-Atg8 and R18 in WT, *atg2*Δ, and *atg2*^{LT} mutant
872 cells. The scale bar represents 5 μm. Graphs represent the line profiles of the
873 fluorescence intensity from the images on the left.
874 (D) Percentage of colocalization calculated using 100 cells from 3 independent
875 experiments in (C). Error bars represent SD. P-values were calculated using two-way
876 ANOVA.
877 (E) IM (mNG–Atg8) is labeled with R18 in prApe1-overexpressing WT cells and
878 visualized under the confocal microscope. The square indicates the area that was
879 photobleached. The scale bar represents 5 μm.
880 (F) FRAP analysis. Images were captured at the indicated time points. The scale bar
881 represents 1 μm.
882 (G) Fluorescence recovery of the IM (mNG-Atg8) and R18 after photobleaching.
883 Error bars represent SD; n = 7.
884 (H) Quantification of the length of the IM at 0 and 320 s. p-values were calculated
885 using multiple unpaired t-tests.

Figure 5

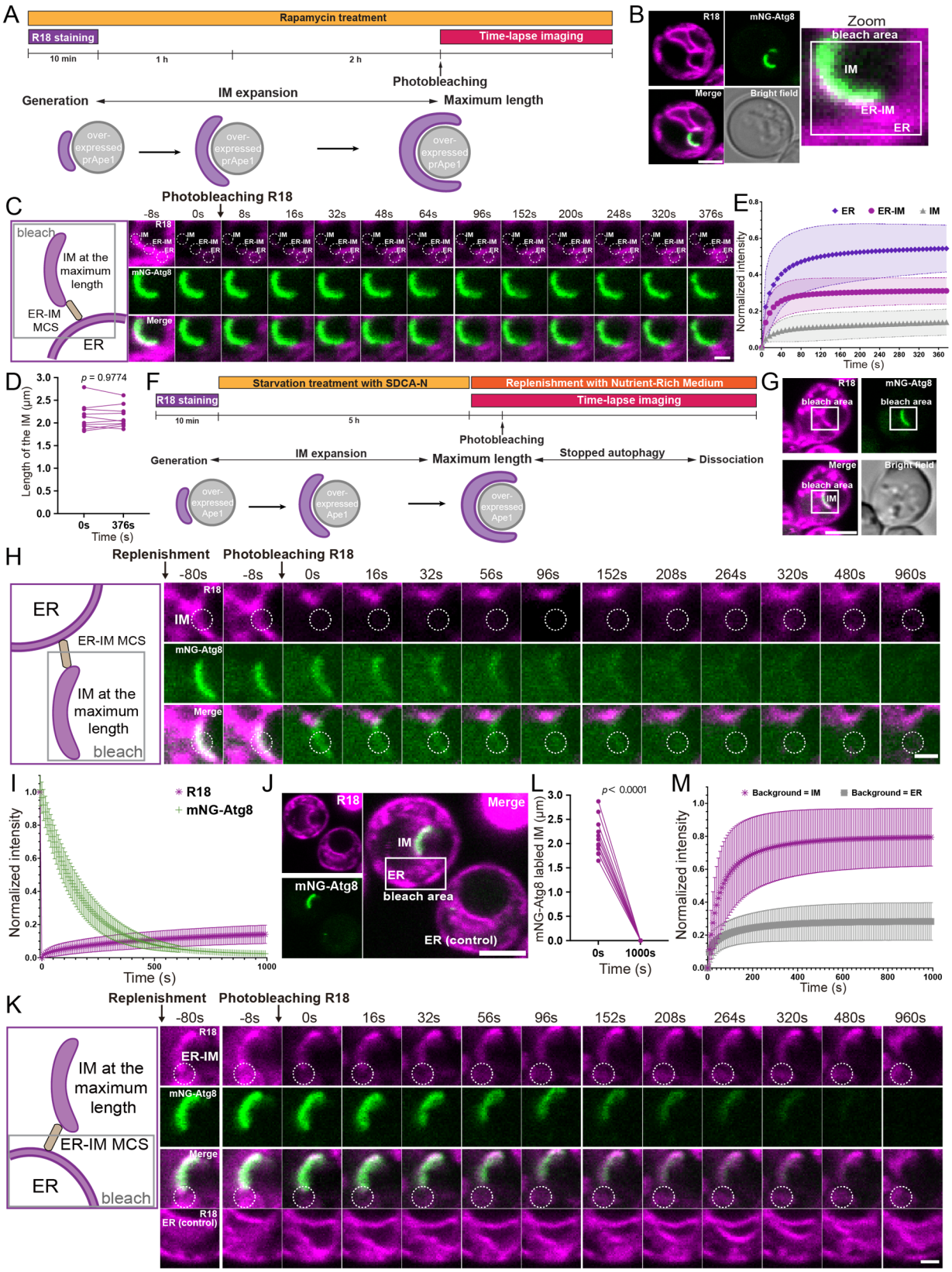
A
Rapamycin treatment
R18 staining
Time-lapse imaging
10 min
1 h
2 h
Photobleaching
Generation
IM expansion
Maximum length
over-expressed prApe1
B
R18
mNG-Atg8
Merge
Bright field
Zoom
bleach area
IM
ER-IM
ER
C
Photobleaching R18
-8s
0s
8s
16s
32s
48s
64s
96s
152s
200s
248s
320s
376s
bleach
IM at the maximum length
ER-IM MCS
ER
mNG-Atg8
Merge
E
ER
ER-IM
IM
Normalized intensity
Time (s)
D
p = 0.9774
Length of the IM (μm)
0s
376s
Time (s)
F
Starvation treatment with SDCA-N
Replenishment with Nutrient-Rich Medium
R18 staining
Time-lapse imaging
10 min
5 h
Photobleaching
Generation
IM expansion
Maximum length
Stopped autophagy
Dissociation
over-expressed Ape1
G
R18
mNG-Atg8
bleach area
Merge
Bright field
IM
H
Replenishment
Photobleaching R18
-80s
-8s
0s
16s
32s
56s
96s
152s
208s
264s
320s
480s
960s
ER
ER-IM MCS
IM at the maximum length
bleach
R18
IM
mNG-Atg8
Merge
I
R18
mNG-Atg8
Normalized intensity
Time (s)
J
R18
Merge
IM
ER
bleach area
mNG-Atg8
ER (control)
L
p< 0.0001
mNG-Atg8 labled IM (μm)
0s
1000s
Time (s)
M
Background = IM
Background = ER
Normalized intensity
Time (s)
K
Replenishment
Photobleaching R18
-80s
-8s
0s
16s
32s
56s
96s
152s
208s
264s
320s
480s
960s
IM at the maximum length
ER-IM MCS
ER
bleach
R18
ER-IM
mNG-Atg8
Merge
R18
ER (control)

886 **Figure 5 Phospholipids are transferred from the IM back to the ER after the**
887 **termination of autophagy.**
888 (A) Procedure for the experiment in (C). prApe1-overexpressed cells were treated with
889 rapamycin, and the FRAP analysis was performed as indicated.
890 (B) The IM (mNG–Atg8) is labeled with R18 in prApe1-overexpressing WT cells under
891 the confocal microscope. The square indicates the area that is to be photobleached in
892 (C). The scale bar represents 2 μm.
893 (C) Schematic drawing of the photobleached area (left). During the FRAP analysis,
894 the fluorescence intensity of R18 at three points (ER, ER–IM, and IM) was monitored
895 (right). Images were captured as indicated. The scale bar represents 1 μm.
896 (D) Quantification of the length of the IM after reaching a maximum length. P-values
897 were calculated using multiple unpaired t-tests.
898 (E) Fluorescence recovery of R18 at the IM, ER–IM, and ER after photobleaching.
899 Error bars represent SD; n = 7.
900 (F) The procedure for the experiments in (H and K). prApe1-overexpressing cells were
901 starved in SDCA-N medium for 5 h, and nutrient-rich medium was then added to
902 terminate autophagy, followed by FRAP analysis as indicated.
903 (G) IM (mNG–Atg8) is labeled with R18 in prApe1-overexpressing WT cells and
904 visualized under a confocal microscope. The square indicates the area that was
905 photobleached in (H). The scale bar represents 2 μm.
906 (H) Schematic drawing of the photobleached area (left). The fluorescence intensities
907 of mNG–Atg8 and R18 at the IM were monitored (right). Images were captured as
908 indicated. The scale bar represents 1 μm.
909 (I) Fluorescence recovery of mNG-Atg8 and R18 at the IM after photobleaching.
910 Error bars represent SD; n = 7.
911 (J) IM (mNG–Atg8) is labeled with R18 in prApe1-overexpressing WT cells and
912 visualized under a confocal microscope. The square indicates the area that was
913 photobleached in (K). The scale bar represents 5 μm.
914 (K) Schematic drawing of the photobleached area (left). The fluorescence intensity of
915 R18 at the ER–IM MCS was monitored (right). The scale bar represents 1 μm.
916 (L) Quantification of the length of the IM after nutrient-rich medium repletion in (H) and
917 (K). p-values were calculated using multiple unpaired t-tests.
918 (M) Fluorescence recovery of R18 at the ER–IM MCS, calculated using the IM and
919 unbleached ER as background references. Error bars represent SD; n = 7.

Figure 6

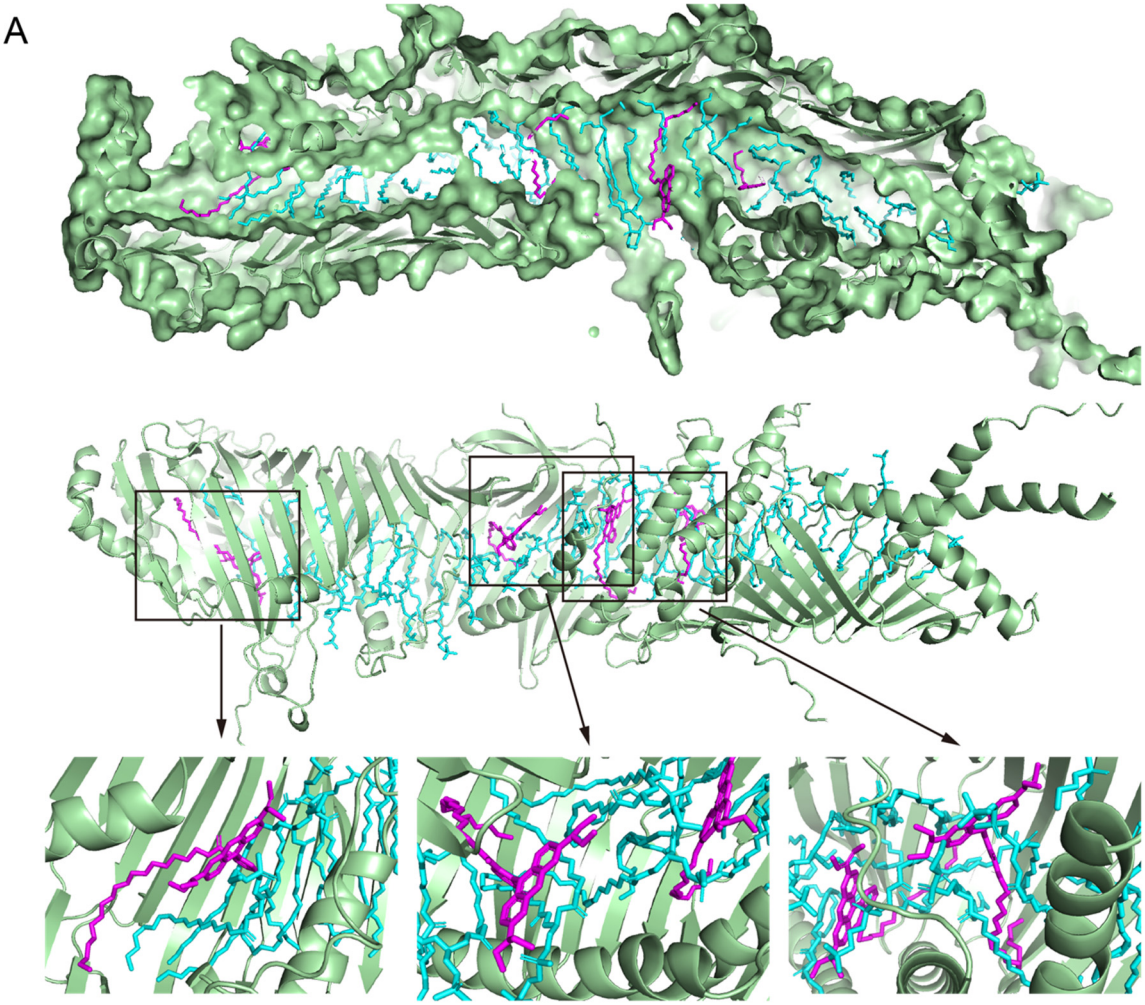
A

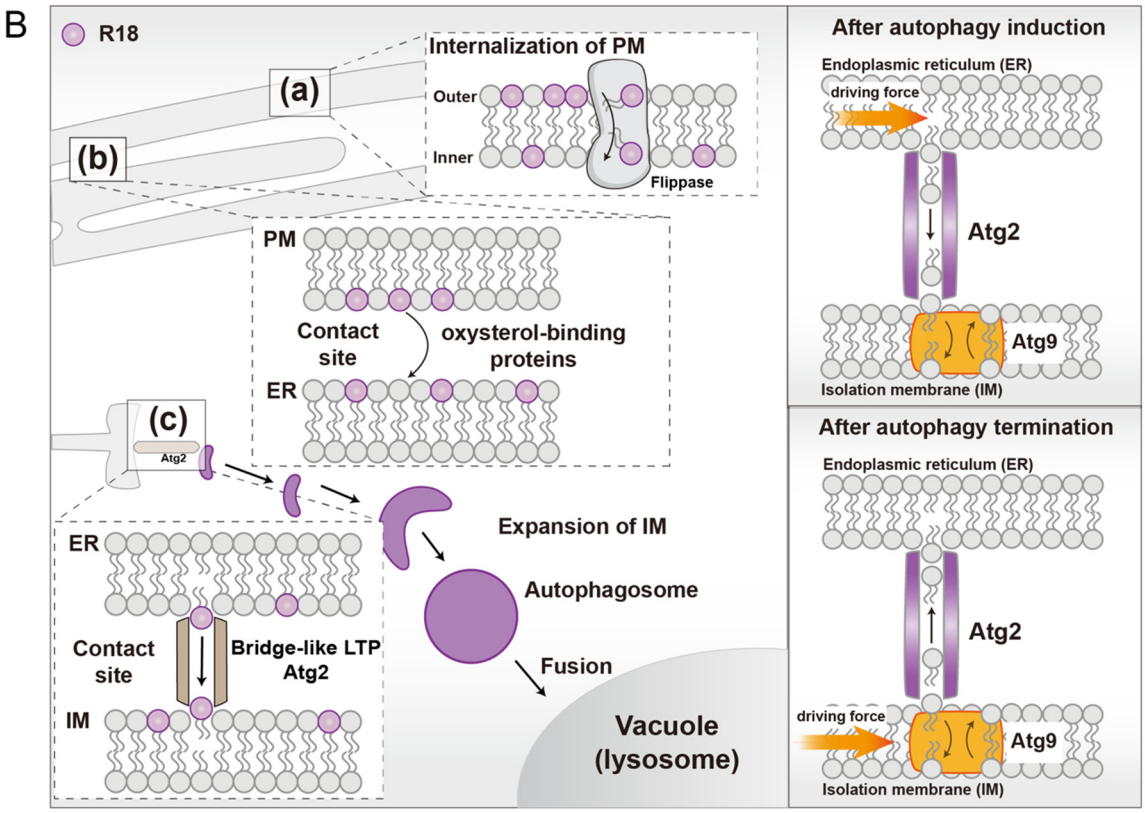
B
R18
(a)
(b)
(c)
Atg2
Internalization of PM
Outer
Inner
Flippase
PM
Contact site
oxysterol-binding proteins
ER
ER
Contact site
Bridge-like LTP Atg2
IM
Expansion of IM
Autophagosome
Fusion
Vacuole (lysosome)
After autophagy induction
Endoplasmic reticulum (ER)
driving force
Atg2
Atg9
Isolation membrane (IM)
After autophagy termination
Endoplasmic reticulum (ER)
Atg2
driving force
Atg9
Isolation membrane (IM)

Figure 6 Models for R18 transport from the PM to the IM.

(A) AlphaFold3 model containing Atg2 (1–1346), 12×POPC, 12×DOPE and 4×R18. Cyan represents POPC and DOPE, and magenta represents R18.

(B) Models of the R18 transfer route to the IM (left). Reversible one-way lipid transfer model of Atg2 (right).

Supplemental Information

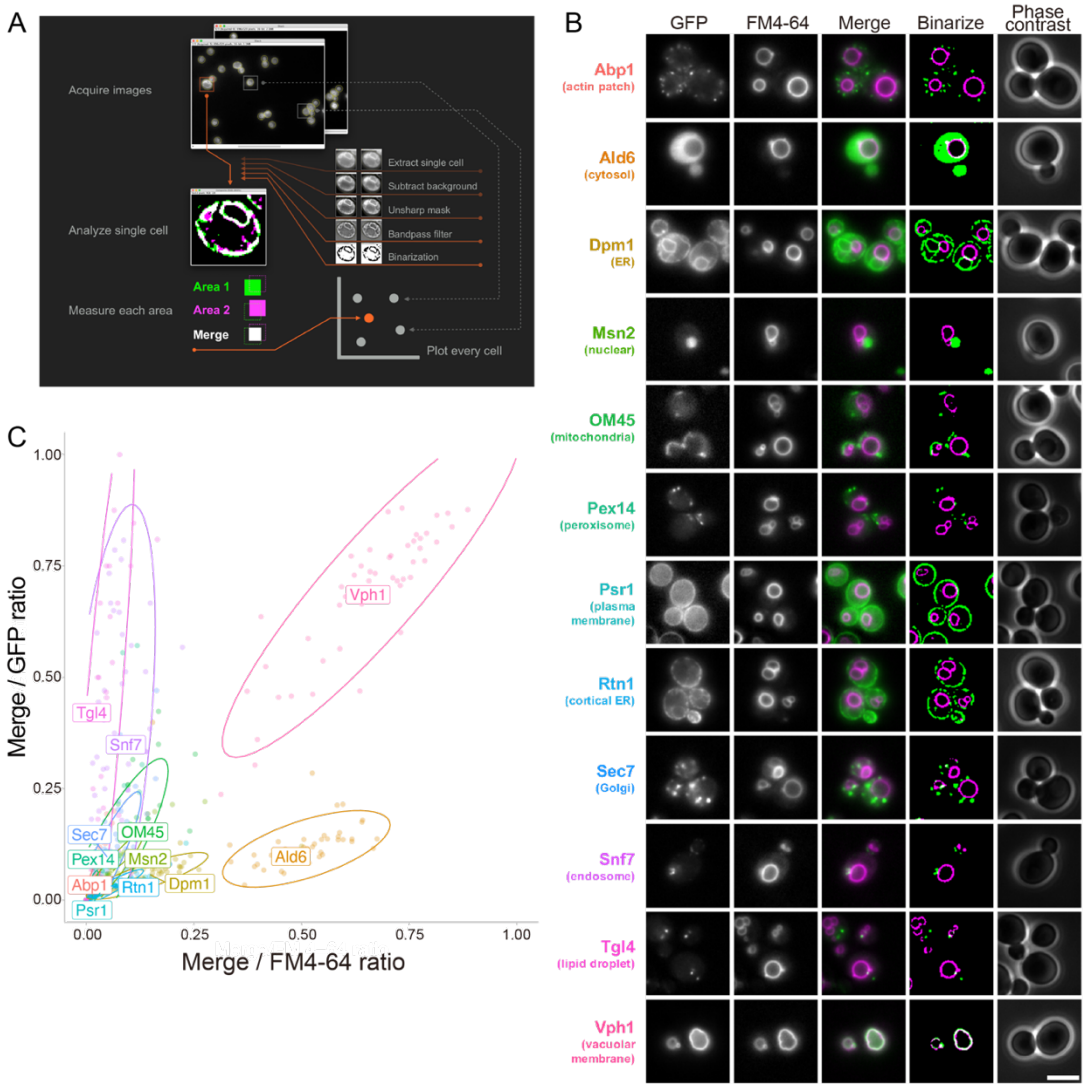

Figure S1. FM4-64 selectively labels the vacuole membrane

(A) Single-cell images were extracted from the acquired images. Background brightness was subtracted using the rolling ball algorithm. Images were sharpened using unsharp masking and filtered with a bandpass filter to detect drastic intensity changes. Each structure was extracted through binarization and subsequently merged. Three areas—each fluorescence-labeled area and merged area—were measured.

(B) Cells expressing GFP-tagged organelle marker proteins were grown in SDCA medium until they reached the mid-log phase and were stained with 8 μM FM4-64. The scale bar represents 5 μm.

(C) Scatter plot of the merge/FM4-64 ratio (x-axis) versus the merge/GFP ratio (y-axis) with a 95% probability ellipse. At least 50 cells were analyzed for each strain.

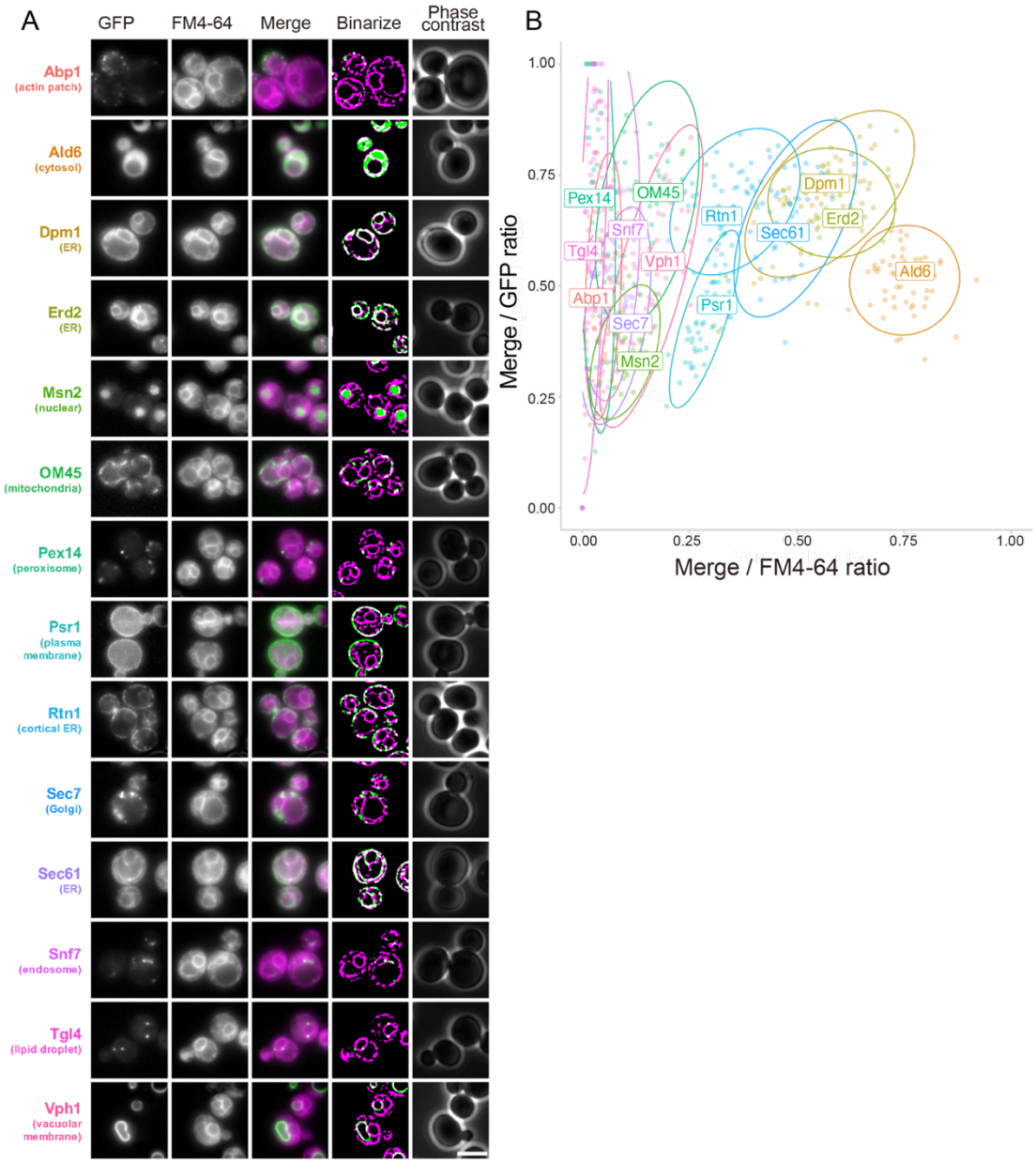

Figure S2. R18 labels the ER membrane

(A) Cell expressing GFP-labeled organelle marker proteins were grown in SDCA medium until they reached the mid-log phase and were stained with 10 µg/mL of R18. (B) Scatter plot of the merge/R18 ratio (x-axis) versus the merge/GFP ratio (y-axis) with a 95% probability ellipse. At least 50 cells were analyzed for each strain. The scale bar represents 5 µm.

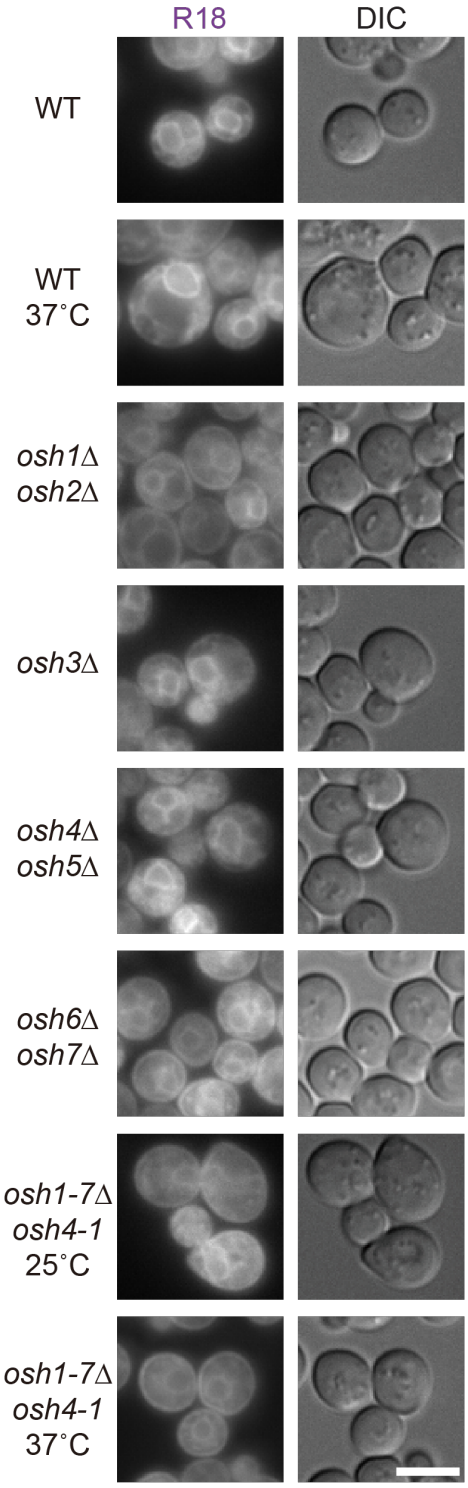

944 **Figure S3. R18 distribution in the Osh mutants**

945 Cells were grown in SDCA medium to the mid-log phase at 25ºC. Then, cells
946 indicated by "37ºC" were preincubated at 37°C for 1 h. The cells were stained with
947 R18 at the indicated temperature for 10 min and then washed with fresh medium. WT,
948 wild-type. DIC, differential interference contrast. The scale bar represents 5 μm.

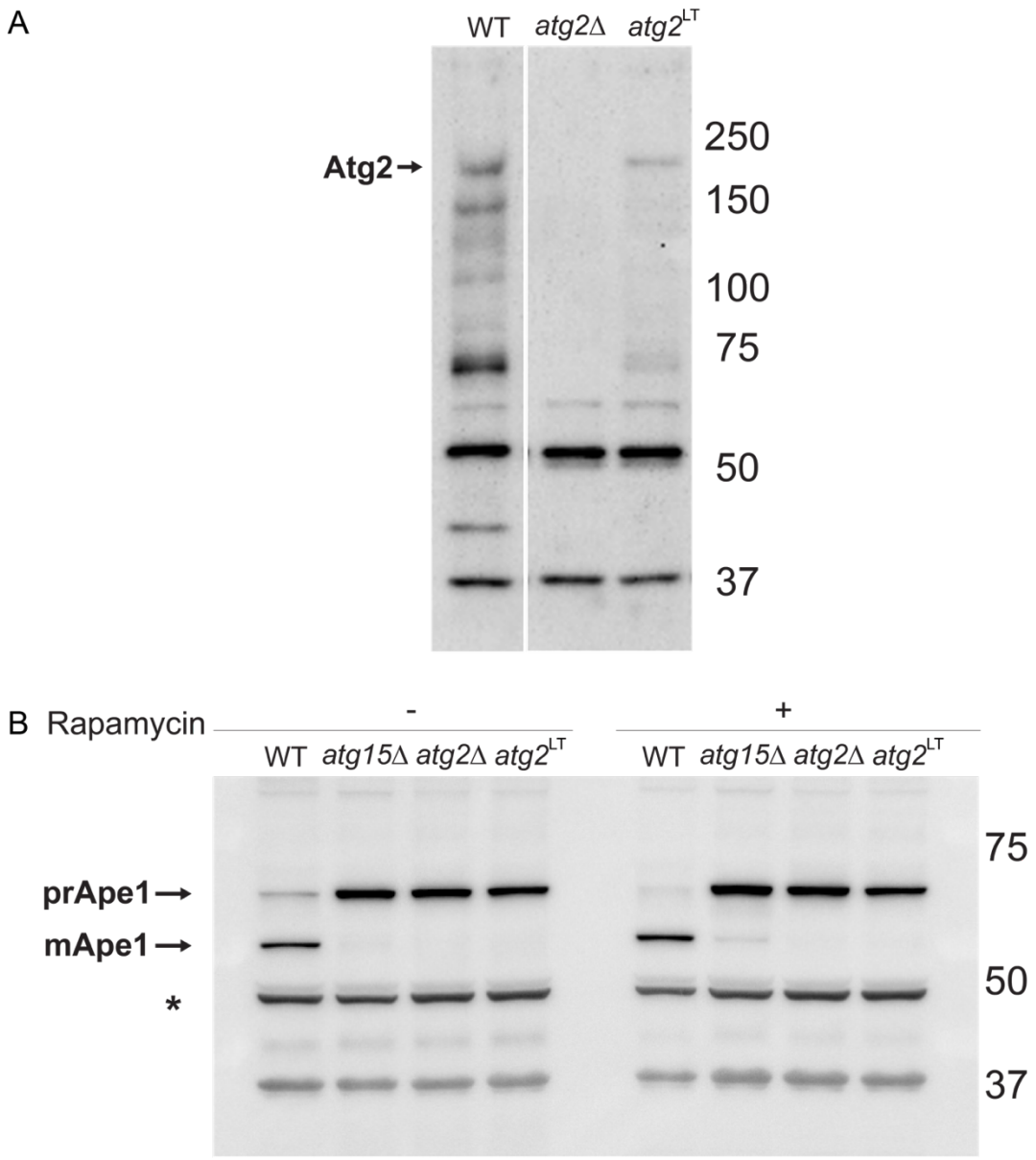

949 **Figure S4. Construction of atg2^{LT} cells.**
950 (A) Immunoblotting analysis was performed using anti-Atg2 antibodies.
951 (B) The same samples are used in (A). Western blot analysis was performed using an
952 anti-Ape1 antibody. The upper bands represent precursor Ape1 (prApe1), the middle
953 bands represent mature Ape1 (mApe1), and the lower bands represent nonspecific
954 signals that can be used as an internal control (*).

955 **Table S1.** *S. cerevisiae* strains used in this study

956

Strain[a]	Mat	Genotype	Source
BY4741	α	*his3Δ1 leu2Δ0 met15Δ0 ura3Δ0*	(S1)
W303-1A	α	*ade2-1 leu2-3 his3-11, 15 trp1-1 ura3-1 can1-100*	This study
SEY6210	α	*lys2 suc2 his3 leu2 trp1 ura3*	(S2)
YHL1	α	SEY6210 *atg2Δ::LEU2*	This study
YHL2	α	SEY6210 *atg15Δ::hphNT1*	This study
YHL3	α	SEY6210 *pep4Δ::LEU2*	This study
YKM674	α	SEY6210 *atg39Δ::zeoNT3 atg40Δ::hphNT1*	(S3)
YOC5565	α	SEY6210 *atg39Δ::zeoNT3 atg40Δ::hphNT1 atg15Δ::natNT2*	This study
YCK445	α	SEY6210; *DPM1-YEGFP-kanMX*	(S4)
YHL4	α	W303-1A *atg2Δ::natNT2*	This study
YHL5	α	W303-1A *atg15Δ::KANMX6*	This study
YKT38	a	*ura3-52 his3-200 trp1-63 leu2-1 lys2-801*	(S5)
YKT715	α	YKT38 *lem3Δ::TRP1*	(S6)
YKT917	α	YKT38 *dnf3Δ::HIS3MX6*	(S7)
YKT1660	a	YKT38 *KanMX6::P_{GAL1}-3HA-NEO1*	(S8)
YHL6	α	YKT38 *mNeonGreen-ATG8::LEU2*	This study
YHL9 (*atg2*^{LT})	α	YKT38 *atg2*$^{F88R\ G97S\ L180E\ L208R\ L311E}$ *mNeonGreen-ATG8::LEU2*	This study
Abp1-GFP	α	BY4741 *abp1Δ::ABP1-GFP:HIS3MX6*	(S9)
Ald6-GFP	α	BY4741 *ald6Δ::ALD6-GFP:HIS3MX6*	(S9)
Dpm1-GFP	α	BY4741 *dpm1Δ::DPM1-GFP:HIS3MX6*	(S9)
Erd2-GFP	α	BY4741 *erd2Δ::ERD2-GFP:HIS3MX6*	(S9)
Msn2-GFP	α	BY4741 *msn2Δ::MSN2-GFP:HIS3MX6*	(S9)
OM45-GFP	α	BY4741 *om45Δ::OM45-GFP:HIS3MX6*	(S9)
Pex14-GFP	α	BY4741 *pex14Δ::PEX14-GFP:HIS3MX6*	(S9)
Psr1-GFP	α	BY4741 *psr1Δ::PSR1-GFP:HIS3MX6*	(S9)
Rtn1-GFP	α	BY4741 *rtn1Δ::RTN1-GFP:HIS3MX6*	(S9)
Sec7-GFP	α	BY4741 *sec7Δ::SEC7-GFP:HIS3MX6*	(S9)
Sec61-GFP	α	BY4741 *sec61Δ::SEC61-GFP:HIS3MX6*	(S9)
Snf7-GFP	α	BY4741 *snf7Δ::SNF7-GFP:HIS3MX6*	(S9)
Tgl4-GFP	α	BY4741 *tgl4Δ::TGL4-GFP:HIS3MX6*	(S9)
Vph1-GFP	α	BY4741 *vph1Δ::VPH1-GFP:HIS3MX6*	(S9)
RY6222	α	SEY6210 *osh1Δ::URA3 osh2Δ::URA3*	(S10)
JRY6202	α	SEY6210 *osh3Δ::LYS2*	(S10)
JRY6227	α	SEY6210 *osh4Δ::HIS3 osh5Δ::LEU2*	(S10)
JRY6207	α	SEY6210 *osh6Δ::LEU2 osh7Δ::HIS3*	(S10)
CBY926	α	SEY6210 *osh1Δ::kanMX4 osh2Δ::kanMX4 osh3Δ::LYS2 osh4Δ::HIS3 osh5Δ::LEU2 osh6Δ::LEU2 osh7Δ::HIS3 osh4-1-TRP*	(S11)

957 [a]: YKT strains are isogenic derivatives of YEF473 (S12).

958 **Table S2.** Plasmids used in this study

Name	Properties	Marker	Source
pYEX-BX[prApe1]	Plasmid for the expression of prApe1 from the *CUP*1 promoter	*URA3*	(S4)
pRS314[GFP-Atg8]	Plasmid for the expression of GFP-Atg8	*URA3*	(S13)
pRS305[mNeonGreen-Atg8]	Plasmid for the integration of mNeonGreen-Atg8	*LEU2*	(S14)
pCB255	Plasmid for the expression of *osh4-1*	*TRP1*	(S10)

959 References

960 S1. Brachmann, C. B. *et al*. Designer deletion strains derived from *Saccharomyces*
961 *cerevisiae* S288C: a useful set of strains and plasmids for PCR-mediated gene
962 disruption and other applications. *Yeast* **14**, 115–132 (1998).

963 S2. Robinson, J. S., Klionsky, D. J., Banta, L. M. & Emr, S. D. Protein sorting in
964 *Saccharomyces cerevisiae*: isolation of mutants defective in the delivery and
965 processing of multiple vacuolar hydrolases. *Mol Cell Biol* **8**, 4936–4948 (1988).

966 S3. Mochida, K. *et al*. Receptor-mediated selective autophagy degrades the
967 endoplasmic reticulum and the nucleus. *Nature* **522**, 359–362 (2015).

968 S4. Suzuki, K., Kubota, Y., Sekito, T. & Ohsumi, Y. Hierarchy of Atg proteins in pre-
969 autophagosomal structure organization. *Genes to Cells* **12**, 209–218 (2007).

970 S5. Misu, K. *et al*. Cdc50p, a Conserved Endosomal Membrane Protein, Controls
971 Polarized Growth in Saccharomyces cerevisiae. *Mol Biol Cell* **14**, 730–747 (2003).

972 S6. Saito, K. *et al*. Cdc50p, a protein required for polarized growth, associates with
973 the Drs2p P-type ATPase implicated in phospholipid translocation in Saccharomyces
974 cerevisiae. *Mol. Biol. Cell* **15**, 3418–3432 (2004).

975 S7. Kishimoto, T. *et al*. Phospholipid flippases and Sfk1 are essential for the retention
976 of ergosterol in the plasma membrane. *Mol Biol Cell* **32**, 1374–1392 (2021).

977 S8. Takeda, M., Yamagami, K. & Tanaka, K. Role of Phosphatidylserine in
978 Phospholipid Flippase-Mediated Vesicle Transport in Saccharomyces cerevisiae.
979 *Eukaryot Cell* **13**, 363–375 (2014).

980 S9. Huh, W. *et al*. Global analysis of protein localization in budding yeast. *Nature*
981 **425**, 686–691 (2003).

982 S10. Beh, C. T. & Rine, J. A role for yeast oxysterol-binding protein homologs in
983 endocytosis and in the maintenance of intracellular sterol-lipid distribution. *Journal of*
984 *Cell Science* **117**, 2983–2996 (2004).

985 S11. Tian, S., Ohta, A., Horiuchi, H. & Fukuda, R. Oxysterol-binding protein
986 homologs mediate sterol transport from the endoplasmic reticulum to mitochondria in
987 yeast. *Journal of Biological Chemistry* **293**, 5636–5648 (2018).

988 S12. Longtine, M. S. et al. Additional modules for versatile and economical PCR-
989 based gene deletion and modification in Saccharomyces cerevisiae. Yeast **14**, 953–
990 961 (1998).

991 S13. Suzuki, K. *et al*. The pre-autophagosomal structure organized by concerted
992 functions of *APG* genes is essential for autophagosome formation. *EMBO J* **20**,
993 5971–5981 (2001).

994 S14. Hirata, E., Ohya, Y. & Suzuki, K. Atg4 plays an important role in efficient
995 expansion of autophagic isolation membranes by cleaving lipidated Atg8 in
996 *Saccharomyces cerevisiae*. *PLoS One* **12**, e0181047 (2017).